ARTICLE IN PRESS

Available online at www.sciencedirect.com
SCIENCE DIRECT®

Journal of Computational Physics xxx (2005) xxx–xxx

JOURNAL OF COMPUTATIONAL PHYSICS

www.elsevier.com/locate/jcp

Numerical studies of the stochastic Korteweg-de Vries equation

Guang Lin, Leopold Grinberg, George Em Karniadakis *

Division of Applied Mathematics, Brown University, 182 George Street, Box F, Providence, RI 02912, USA

Received 10 March 2005; received in revised form 21 August 2005; accepted 30 August 2005

Abstract

We present numerical solutions of the stochastic Korteweg-de Vries equation for three cases corresponding to additive time-dependent noise, multiplicative space-dependent noise and a combination of the two. We employ polynomial chaos for discretization in random space, and discontinuous Galerkin and finite difference for discretization in physical space. The accuracy of the stochastic solutions is investigated by comparing the first two moments against analytical and Monte Carlo simulation results. Of particular interest is the interplay of spatial discretization error with the stochastic approximation error, which is examined for different orders of spatial and stochastic approximation.

Keywords: Uncertainty; Polynomial chaos; Discontinuous Galerkin method; KdV

1. Introduction

It is well known that the often-studied Korteweg-de Vries (KdV) equation is a good model for describing wave phenomena in plasma dynamics. In 1966, Washimi and Taniuti [1] established rigorously that the KdV equation governs the propagation of small-amplitude ion-accoustic waves. The stochastic KdV equation describes *noisy* plasmas, and it has been studied mostly theoretically in the last two decades, see [2–6]. Zabusky and Kruskal [7] first discovered the stability properties of the solitons exhibited by certain nonlinear differential equations in their classical study, and the findings were confirmed later by the theory developed by Gardner and co-workers [8]. Wadati [2] obtained an exact solution for additive time-dependent white Gaussian noise, predicting that the mean single-soliton should behave as a Gaussian packet with width increasing as $t^{3/2}$ and amplitude decreasing as $t^{-3/2}$ at long-time. Later, Wadati and Akutsu [9] extended this work and obtained exact multisoliton solutions, discovering that the mean soliton width increases only as $t^{1/2}$. Also, Iizuka [10] obtained the theoretical results for the diffusion of solitons under the effect of multiplicative noise with long range correlation, and Scalerandi and Romano's numerical study [11] confirmed Iizuka's work. An important contribution to the studies of nonlinear random fields was made by the *inverse scattering technique*

* Corresponding author. Tel.: +1 401 863 1217; fax: +1 401 863 3369.
E-mail address: gk@dam.brown.edu (G.E. Karniadakis).

0021-9991/$ - see front matter © 2005 Elsevier Inc. All rights reserved.
doi:10.1016/j.jcp.2005.08.029

(IST). It allows the construction of the exact solvable nonlinear stochastic equations. Different perturbation approaches have been developed on the basis of the IST. Historically, the first nonlinear evolution equation integrated by means of the inverse scattering scheme for KdV equation was presented in [8]. Different foundations of IST are described in [12–17], while how IST is applied to the KdV equation is studied in detail in the books of Konotop and Vazquez [18] and Novikov et al. [19]. Unlike the plethora of the theoretical and perturbation-based works, direct numerical simulation studies of the KdV equation are much fewer, e.g. [4]; this is the main objective of the current work.

In this paper, we investigate the one-dimensional stochastic Korteweg-de Vries (KdV) equation, with homogeneous Dirichlet boundary conditions, in the form:

$$\begin{aligned} &u_t + (-6u + v\zeta(\xi, x))u_x + u_{xxx} = \epsilon\eta(\xi, t), \\ &u(\xi = 0, x, t = 0) = -2\kappa^2 \mathrm{sech}^2(\kappa x), \end{aligned} \tag{1}$$

where ζ and η are the space- and time-dependent random noise with amplitude v and ϵ, respectively, and ξ is a random variable.

Specifically, we will present numerical solutions for three cases corresponding to:

- Time-dependent additive noise only, corresponding to setting $v = 0$ in Eq. (1), and
- Space-dependent multiplicative noise only, corresponding to setting $\epsilon = 0$ in Eq. (1).
- A combination of the above two cases, for $v \neq 0$ and $\epsilon \neq 0$.

In the first case, analytical solutions are available and thus it can be used for benchmarking and comparisons of convergence rates and efficiency of numerical solvers. In the second case, we assume that the stochastic term is active only in a small region located approximately in the middle of the domain. No analytical solutions are available but we perform Monte Carlo simulations to verify the new numerical solvers. Similarly, we will use Monte Carlo simulations to verify our results in the combined case. Typical mean solutions for the first two cases are plotted in Fig. 1. In the additive noise case, the mean solution decays quite fast while in the multiplicative noise case, small ripples – due to dispersion – are present behind the travelling soliton. In both cases, the effect of stochasticity is rather pronounced, and the solitons look quite different from their deterministic counterparts. Specific details on the results and the values of the correlation parameters will be presented in the next section.

The numerical solvers we develop are based on the polynomial chaos (PC) decompositions pioneered by Wiener [20]; stochasticity is represented by a spectral expansion based on Hermite orthogonal polynomials in terms of Gaussian random variables ξ. Ghanem and Spanos [21] were the first to couple PC representations with constraints in solving stochastic PDEs and laid the foundation for the numerical resolution of stochastic PDEs. This approach was extended in [22] for handling non-Gaussian stochastic inputs. The polynomial chaos representation combined with Galerkin projection leads to a *deterministic* system of "KdV-like" equations. To solve the new equations we employ two different discretization approaches. The first one is based on a spectral/hp element discontinuous Galerkin (DG) method [23,24], and the second one on the second-order finite difference method [25].

The primary objective of the current work is to investigate how discretization errors and stochastic approximation errors affect the overall accuracy of the stochastic solution. We will also study the influence of time- and space-dependent noise on the propagation of solitons on the *mean* and *variance* of the solution $u(\xi, x, t)$. As we have seen in Fig. 1 stochasticity introduces dissipation and dispersion, and thus we are interested in measuring the *mean* values of the soliton height and width as a function of the amplitude and correlation length of the noise.

The paper is organized as follows: We provide details of the stochastic approximation and spatial discretization in Appendices A and B so that we focus on the most important results in the main text. In Section 2, we first treat the time-dependent additive noise case; in Section 3, we present results for the space-dependent multiplicative noise case, and in Section 4, we study the combined case. In each section, we separate the fully-correlated cases from the partially-correlated cases since the representation of the stochastic inputs as well as the corresponding results is different.

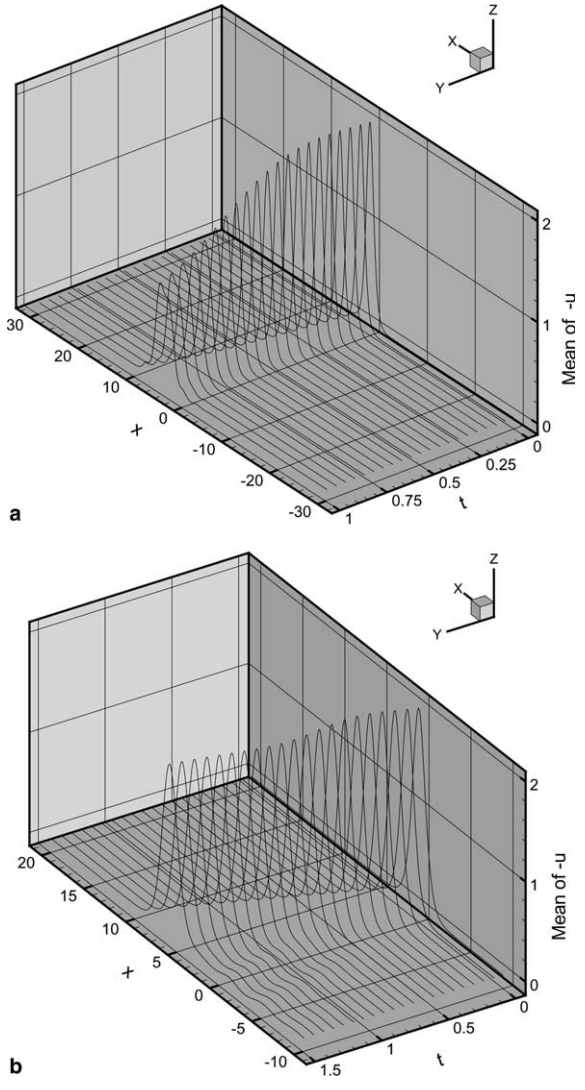

Fig. 1. Spatial distributions of the mean value of $-u(\xi, x, t)$ at different times obtained using the discontinuous Galerkin/Polynomial Chaos (DG/PC) method. (a) Time-dependent random process characterized by correlation length $A = 1$ and additive-noise amplitude $\epsilon = 0.5$. (b) Space-dependent random process characterized by correlation parameters $L = 2$, $A/L = 1$ and multiplicative-noise amplitude $v = 6$.

2. Time-dependent additive noise

The specific stochastic KdV equation we consider in the first case with time-dependent noise and homogeneous Dirichlet boundary conditions is obtained by setting $v = 0$ in Eq. (1),

$$\begin{aligned} &u_t - 6uu_x + u_{xxx} = \epsilon\eta(\boldsymbol{\xi}, t), \quad x \in (-\infty, \infty), \\ &u(\boldsymbol{\xi} = 0, x, t = 0) = -2\kappa^2 \mathrm{sech}^2(\kappa x), \end{aligned} \tag{2}$$

where κ is the wave number. In our simulations, we assume $\kappa = 1$. The initial height of the soliton is $h = 2\kappa^2 = 2$, and the one-dimensional computational domain is defined by $x \in [-30, 30]$. The inhomogeneous term $\eta(\boldsymbol{\xi}, t)$ represents the external time-dependent noise. The one-soliton exact solution for Eq. (2) was first derived in [2]. Let us assume that the time-dependent additive noise $\eta(\boldsymbol{\xi}, t)$ is integrable in time, i.e.,

$$W(\boldsymbol{\xi},t) \equiv \epsilon \int_0^t \eta(\boldsymbol{\xi},t')\,\mathrm{d}t', \tag{3}$$

and we define

$$U(x,t,\boldsymbol{\xi}) \equiv u(x,t) - W(\boldsymbol{\xi},t).$$

Eq. (2) is then transformed into

$$U_t - 6W(t)U_x - 6UU_x + U_{xxx} = 0. \tag{4}$$

We also define

$$m(\boldsymbol{\xi},t) \equiv 6\int_0^t W(\boldsymbol{\xi},t_1)\,\mathrm{d}t_1$$

and apply the Galilean transformation

$$X = x + m(\boldsymbol{\xi},t).$$

Eq. (4) can then be rewritten as

$$U_t(X,t) - 6U(X,t)U_X(X,t) + U_{XXX}(X,t) = 0. \tag{5}$$

Eq. (5) is a standard KdV equation and the analytical solution is

$$U(X,t) = -2\kappa^2\mathrm{sech}^2\{\kappa(X-ct)\},$$

where $c = 4\kappa^2$ is the wave speed of the soliton. Thus, the original analytical solution is

$$u(x,t,\boldsymbol{\xi}) = W(\boldsymbol{\xi},t) + U(X,t) = W(\boldsymbol{\xi},t) - 2\kappa^2\mathrm{sech}^2\left\{\kappa(x-ct) + 6\kappa\int_0^t W(\boldsymbol{\xi},t_1)\,\mathrm{d}t_1\right\}. \tag{6}$$

The only assumption in the above procedure is that the time-dependent additive noise $\eta(\boldsymbol{\xi},t)$ is integrable in time and no other assumptions or approximations have been made. Thus, the analytical solution (Eq. (6)) can be defined for either white noise, random variable or random process.

From the one-soliton solution Eq. (6), we observe that

$$\mathrm{Max}_{x,\xi,t}\{u(\boldsymbol{\xi},x,t)\} - \mathrm{Min}_{x,\xi,t}\{u(\boldsymbol{\xi},x,t)\} = 2\kappa. \tag{7}$$

Thus, there is no decay of the one-soliton solution for Eq. (2). The shape of the soliton is the same as the solution of the corresponding deterministic KdV equation. However, there is a phase shift $\phi(\xi,t) = -\kappa ct + 6\kappa\int_0^t W(\boldsymbol{\xi},t')\,\mathrm{d}t'$ for each ξ and t. By taking the average over all one-soliton solutions with different phase shift depending on ξ and t, an *effective decay* of the one-soliton *mean* solution is realized.

2.1. Fully-correlated Gaussian noise

A fully-correlated time-dependent noise, η, can be described as a random variable ξ, (i.e., $\eta(\xi) = \xi$), which is a Gaussian random variable with zero mean and unit variance. Thus, we have that $W(t) = \epsilon\xi t$. The exact one-soliton solution in this case is:

$$u(\xi,x,t) = \epsilon\xi t - 2\kappa^2\mathrm{sech}^2\{\kappa(x-ct) + 3\epsilon\kappa\xi t^2\}. \tag{8}$$

The corresponding exact *mean* solution is:

$$\bar{u}(x,t) = \frac{1}{\sqrt{2\pi}}\int_{-\infty}^{\infty} u(\xi,x,t)\mathrm{e}^{-\frac{\xi^2}{2}}\,\mathrm{d}\xi, \tag{9}$$

and the variance is:

$$\mathrm{Var}(u) = \frac{1}{\sqrt{2\pi}}\int_{-\infty}^{\infty} u^2(\xi,x,t)\mathrm{e}^{-\frac{\xi^2}{2}}\,\mathrm{d}\xi - \bar{u}^2. \tag{10}$$

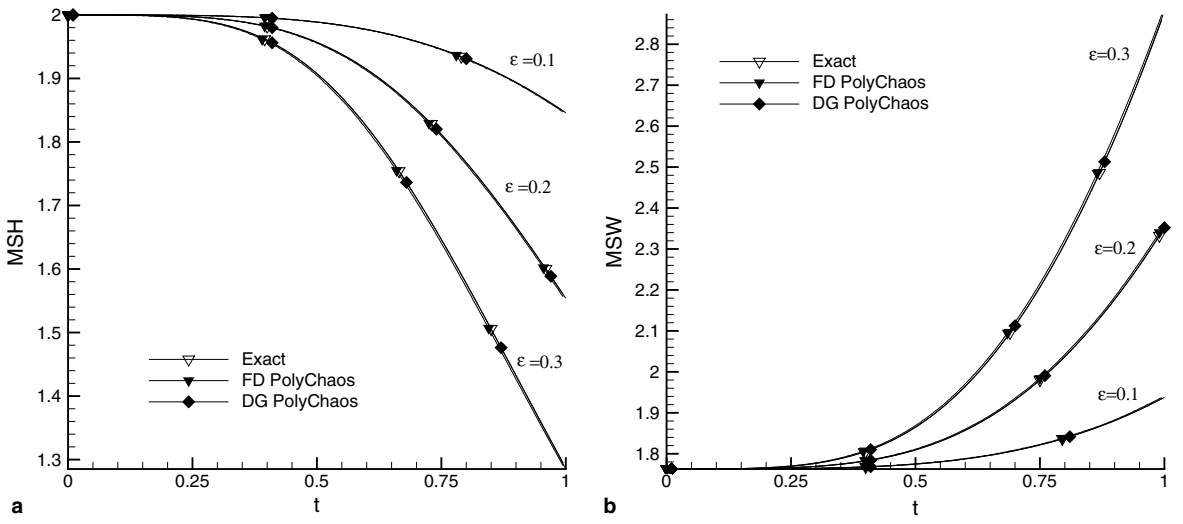

Fig. 2. Fully-correlated case: mean soliton height (MSH) (a) and mean soliton width (MSW) (b) as a function of time for noise amplitudes $\epsilon = 0.1$, 0.2 and 0.3.

We define the *mean soliton height* (MSH) to be $\mathrm{Max}_x|\bar{u}(x,t)|$. We also define the *mean soliton width* (MSW) to be $|x_1 - x_2|$, where x_1 and x_2 satisfy $\bar{u}(x_1,t) = \bar{u}(x_2,t) = \frac{\mathrm{Max}|\bar{u}(x,t)|}{2}$ and $x_1 \neq x_2$. Figs. 2(a) and (b) present the variation of MSH and MSW in time, respectively, for increasing values of the amplitude of the noise. The exact mean solution is computed using Eq. (9) while the polynomial chaos simulations are obtained using eighth-order Hermite polynomials. For spatial discretization, a discontinuous Galerkin (DG) method with 336 degrees-of-freedom (DOF) corresponding to 42 spectral elements with Legendre polynomials of seventh order, and a second-order FD method with 1200 DOF were employed. Good agreement between polynomial chaos simulations and exact mean solutions is observed. Fast decay of MSH as a function of time is observed for increasing values of the amplitude of the noise. Fig. 3 summarizes many simulations indicating the strong correlation between MSH and MSW for different values of ϵ. The results from both the FD/PC and the DG/PC are in good agreement with the exact MSH–MSW correlation.

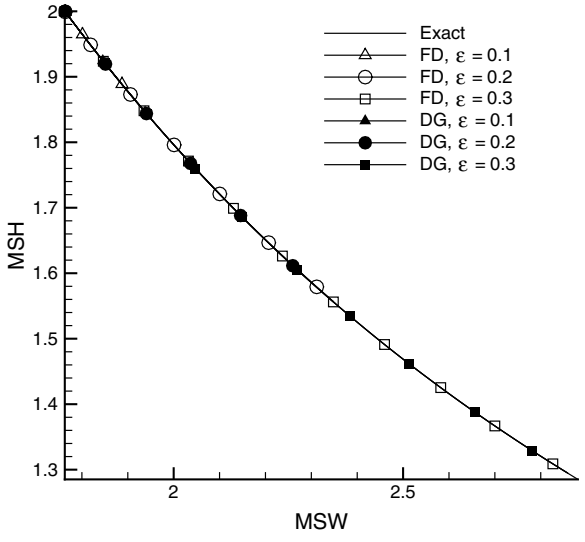

Fig. 3. Correlation between MSH and MSW, obtained by the FD/PC and the DG/PC methods, as time increases from $t = 0$ to 1.

2.1.1. Convergence

We now turn our attention to the convergence of the numerical solution and to the stochastic approximation and spatial discretization errors. We use very small time step in these simulations ($\Delta t \propto 10^{-6}$), thus we can neglect the temporal discretization error in the following comparisons.

Let us denote by $u(\xi, x, t)$ the stochastic solution. By employing Legendre expansions in space and Hermite polynomial chaos expansions in random space, see Appendix A, we have that

$$u(\xi, x, t) = \sum_{j=0}^{K} \sum_{i=0}^{P} \hat{u}_{ij}(t) \Psi_i(x) \phi_j(\xi) + R_s + R_r, \tag{11}$$

where $\Psi_i(x)$ are the Legendre polynomials of order $i = 0, 1, \ldots, P$, $\phi_j(\xi)$ are the Hermite polynomials of order $j = 0, 1, \ldots, K$, and $\hat{u}_{ij}(t)$ are the deterministic coefficients. The numerical error consists of two main components:

(1) The truncation error due to spatial discretization, R_s.
(2) The truncation error due to approximation in random space, R_r.

In Fig. 4, we plot the L_2 error in the mean solution and the variance at $t = 1$ for $\epsilon = 0.1$. Specifically, the L_2 error for the mean and the variance are defined as follows:

$$\begin{aligned} L_2\text{-error}(\bar{u}) &= \sqrt{\sum_{i=1}^{N_T} \frac{(\bar{u}_{\text{num},i} - \bar{u}_{\text{exact},i})^2}{N_T}}, \\ L_2\text{-error}(\text{Var}(u)) &= \sqrt{\sum_{i=1}^{N_T} \frac{(\text{Var}(u)_{\text{num},i} - \text{Var}(u)_{\text{exact},i})^2}{N_T}}. \end{aligned} \tag{12}$$

Here N_T is the total number of grid/quadrature points. The number of degrees-of-freedom (DOF) is based on 30 spectral elements and p-refinement is followed in space, i.e., the number of Legendre polynomials is increased from 6, 8, 10 and 12. With regards to the total error in the mean solution (plot (a)), it is clear that the spatial discretization error dominates for $K \geqslant 3$. For sufficiently high spatio-temporal discretization, exponential convergence with respect to the PC order, K, is obtained. The convergence rate in the variance (plot (b)) does not seem to be affected as strongly by the spatial discretization error. We have included the "exact" solution error in this plot as well; this is the error of the exact stochastic solution represented by $(K+1)$ PC

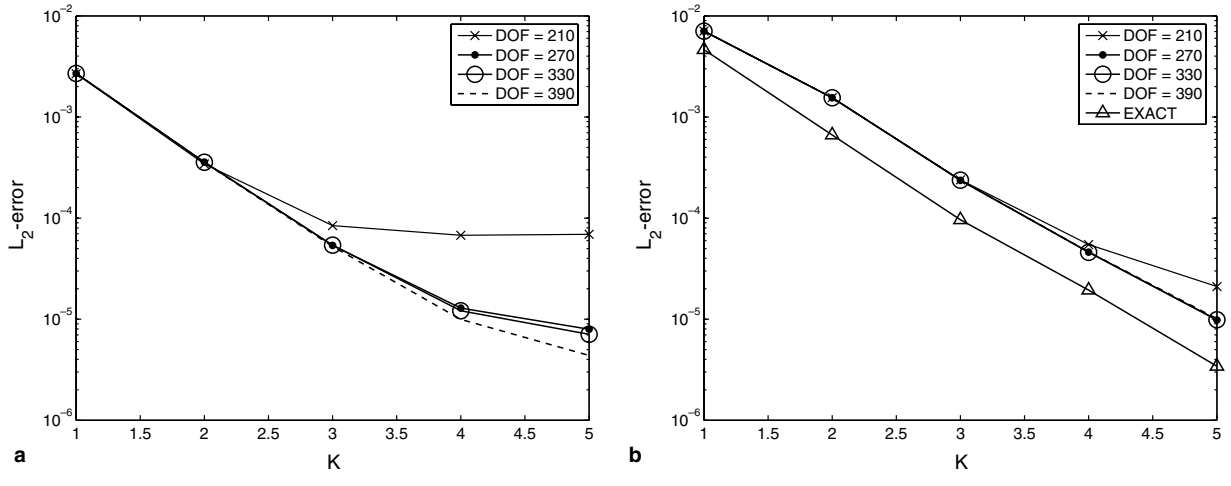

Fig. 4. DG method: convergence rate of L_2-error of the *mean* (a), and *variance* (b) in solving Eq. (1) with ($v = 0, \epsilon = 0.1$), at $t = 1$, with respect to PC order, K for different discretizations (DOF).

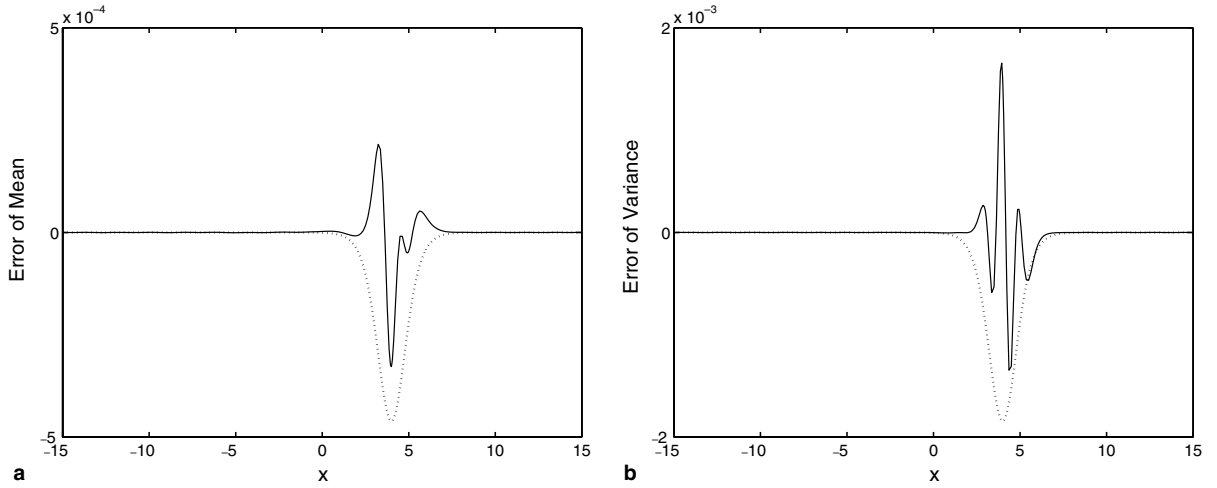

Fig. 5. Pointwise error distribution in the mean (a) and variance (b) for the same conditions as in the previous Fig. 4. The resolution is 30 spectral elements of (Legendre) eighth-order (270 DOF) and PC expansions (Hermite) of third-order.

modes. Therefore, it is not subject to spatio-temporal errors but only to PC approximation error. As we see, the numerical solution of the variance is a *constant* away from the exact solution. In Fig. 5, we plot the pointwise errors in the mean and variance for the resolution indicated in the caption. The solid line denotes the error while the dotted line denotes the position of the scaled soliton. We see that there are no appreciable errors away from the soliton.

2.2. Partially-correlated Gaussian noise

In this section, we assume that η represents partially-correlated time-dependent noise, and it is described by a random process $\eta(\boldsymbol{\xi}, t)$ with zero mean. We also assume that its covariance is given by the exponential kernel, thus:

$$\begin{aligned} &\langle \eta(t,\xi)\rangle = 0, \\ &\langle \eta(t_1,\xi), \eta(t_2,\xi)\rangle = \mathrm{e}^{-\frac{|t_1-t_2|}{A}}, \end{aligned} \tag{13}$$

where A is the correlation length. This covariance kernel describes a first-order Markov process in time.

We approximate the stochastic input via the Karhunen–Loeve decomposition (see [21,22]), i.e., $\eta(\boldsymbol{\xi}, t)$ is approximated by the series:

$$\eta(\boldsymbol{\xi}, t) = \sum_{k=1}^{N} \sqrt{\lambda_k} f_k(t) \xi_k, \tag{14}$$

where N is the number of random dimensions, ξ_k is the Gaussian random variable, λ_k and f_k are the eigenvalues and eigenfunctions of the correlation function, respectively. From Eqs. (3) and (14), we have:

$$W(\boldsymbol{\xi}, t) = \sum_{k=1}^{N} \epsilon \sqrt{\lambda_k} \xi_k \int_0^t f_k(t')\, \mathrm{d}t'. \tag{15}$$

The exact one-soliton solution in this case is:

$$\begin{aligned} u(\xi, x, t) &= W(\xi, t) - 2\kappa^2 \mathrm{sech}^2\left\{\kappa(x - ct) + 6\kappa \int_0^t W(\xi, t')\, \mathrm{d}t'\right\} \\ &= \epsilon \sum_{k=1}^{N} \sqrt{\lambda_k} \xi_k \int_0^t f_k(t')\, \mathrm{d}t' - 2\kappa^2 \mathrm{sech}^2\left\{\kappa(x - ct) + 6\kappa\epsilon \sum_{k=1}^{N} \sqrt{\lambda_k} \xi_k \int_0^t \int_0^{t_1} f_k(t')\, \mathrm{d}t'\, \mathrm{d}t_1\right\}. \end{aligned} \tag{16}$$

Therefore, the exact *mean* solution is readily computed from:

$$\bar{u}(x,t) = \frac{1}{(\sqrt{2\pi})^N} \int_{-\infty}^{\infty} \cdots \int_{-\infty}^{\infty} u(\xi_0, \ldots, \xi_N, x, t) \mathrm{e}^{-\frac{\xi_0^2 + \cdots + \xi_N^2}{2}} \, \mathrm{d}\xi_0 \cdots \mathrm{d}\xi_N. \tag{17}$$

Correspondingly, the exact *variance* is computed from:

$$\mathrm{Var}(u) = \frac{1}{(\sqrt{2\pi})^N} \int_{-\infty}^{\infty} \cdots \int_{-\infty}^{\infty} u^2(\xi_0, \ldots, \xi_N, x, t) \mathrm{e}^{-\frac{\xi_0^2 + \cdots + \xi_N^2}{2}} \, \mathrm{d}\xi_0 \cdots \mathrm{d}\xi_N - \bar{u}^2. \tag{18}$$

Fig. 1(a) (see Section 1) depicts the mean values of $-u(\xi, x, t)$ for time up to $t = 1$, with correlation length $A = 1$ and amplitude $\epsilon = 0.5$. In Fig. 6, we plot the mean and variance of $u(\xi, x, t)$ at $t = 1.0$ for correlation length $A = 1$ and amplitude $\epsilon = 0.1$. The dots represent the simulation results obtained by a DG/PC method. A four-dimensional ($N = 4$) Karhunen–Loeve expansion was used to represent the stochastic input while third-order PC expansions were employed to represent the solution. For the DG discretization we employed 42 spectral elements with Legendre expansions of sixth-order (378 DOF). We also include in the plots the exact solution, denoted by solid line, obtained from Eqs. (17) and (18). Good agreement is observed between the DG/PC results and the exact solutions.

Next, we study the effects of noise amplitude and correlation length on the stochastic soliton. Fig. 7(a) shows how the mean soliton height (MSH) decays with time for different values of the noise amplitude, ϵ. Fig. 7(b) shows the corresponding plot for the mean soliton width (MSW). The discretization employed consists of 42 spectral elements of eighth-order for the DG, and 1200 grid points for the FD method. In random space we used $N = 4$ Karhunen–Loeve modes and the Hermite polynomial was of third-order in the PC expansion. The results are in good agreement (both the FD/PC and the DG/PC) with the exact solutions except at the large amplitude $\epsilon = 0.5$. We performed a similar parametric study but with respect to the correlation length A for fixed value of the amplitude at $\epsilon = 0.3$. Fig. 8(a) shows the decrease of MSH as a function of time, while Fig. 8(b) shows the increase of MSW as a function of time. Here we maintained the same spatial resolution for the DG as before but we increased the number of Karhunen–Loeve modes from $N = 3$ for $A = 10$, to $N = 4$ for $A = 1$ and $N = 9$ for $A = 0.1$. Increasing the correlation length A of the external random noise leads to a faster decay of the soliton, see Fig. 8(a). We summarize several simulation results in Fig. 9 from the two different methods, the DG/PC and the FD/PC, in the height-versus-width plot. The numerical results are in good agreement with the exact solution. We have also investigated the convergence rate for time-dependent additive noise, described as a random process with amplitude $\epsilon = 0.3$. We use DG discretization in

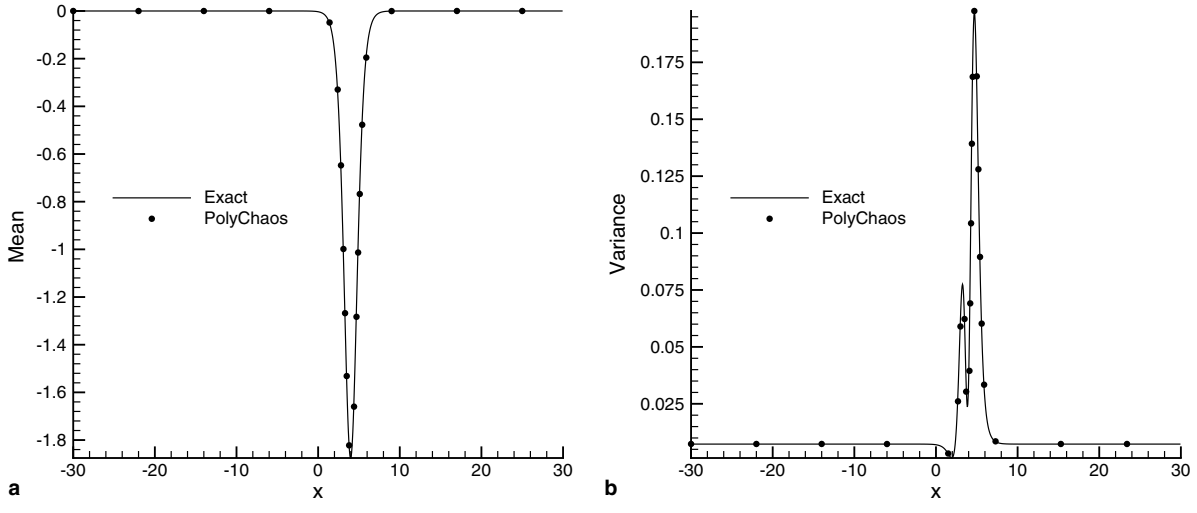

Fig. 6. Mean (a) and variance (b) of $u(\xi, x, t)$ obtained by the DG/PC method at $t = 1.0$ for correlation length $A = 1$, amplitude $\epsilon = 0.1$. The solid line represents the exact solution and the dots denote results from the DG/PC simulation.

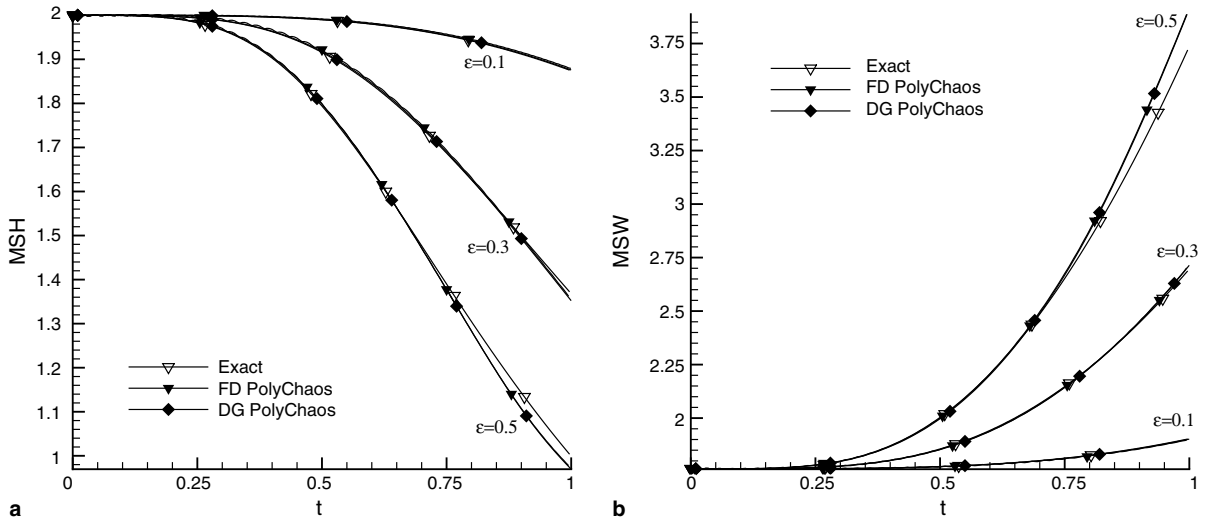

Fig. 7. Mean soliton height (MSH) (a) and mean soliton width (MSW) (b) as a function of time. Time-dependent random noise, described as a random process with correlation length $A = 1$ and amplitude values $\epsilon = 0.1$, 0.3 and 0.5.

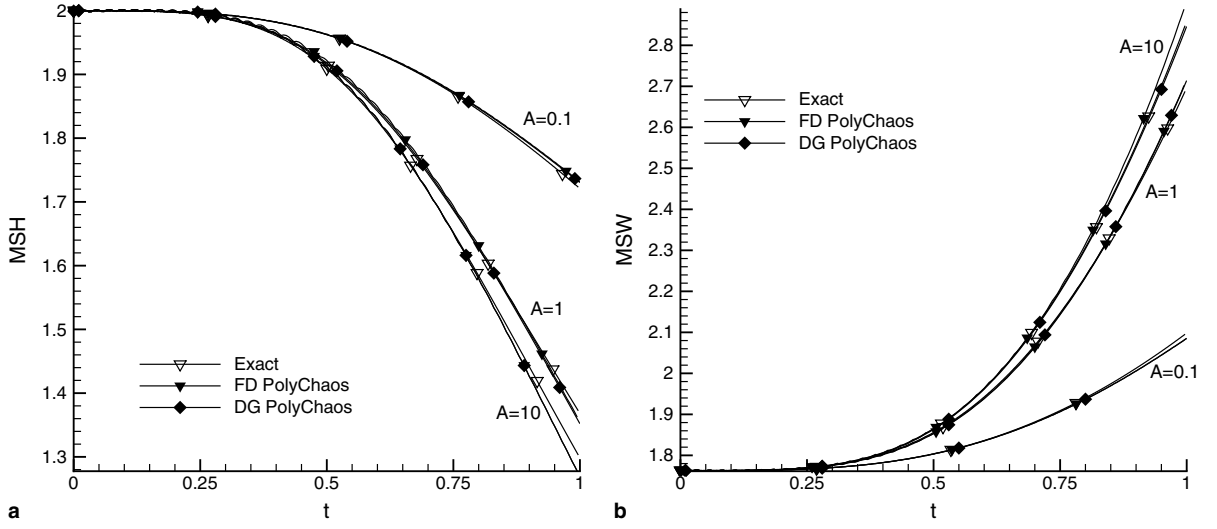

Fig. 8. MSH (a) and MSW (b) as a function of time. Time-dependent random noise, described as a random process with amplitude $\epsilon = 0.3$ and correlation length $A = 0.1$, 1 and 10.

space (with variable Jacobi polynomial orders in each element) and first-order predictor–corrector scheme in time with $\Delta t = 10^{-5}$. Specifically, the L_∞ error of the mean and the variance for this case is defined as follows:

$$\begin{aligned} L_\infty(\bar{u}) &= \mathrm{Max}(\bar{u}_{\mathrm{num},i} - \bar{u}_{\mathrm{exact},i}) \quad \text{for } i = 0, \ldots, N_\mathrm{T}, \\ L_\infty(\mathrm{Var}(u)) &= \mathrm{Max}(\mathrm{Var}(u)_{\mathrm{num},i} - \mathrm{Var}(u)_{\mathrm{exact},i}) \quad \text{for } i = 0, \ldots, N_\mathrm{T}. \end{aligned} \tag{19}$$

Here N_T is the total number of quadrature points in the DG discretization. The exact mean and variance solutions are computed from Eqs. (17) and (18). In Fig. 10 we plot these L_∞ errors versus the PC order K. We observe that in this semi-log plot, exponential convergence is observed, even with this large amplitude of $\epsilon = 0.3$.

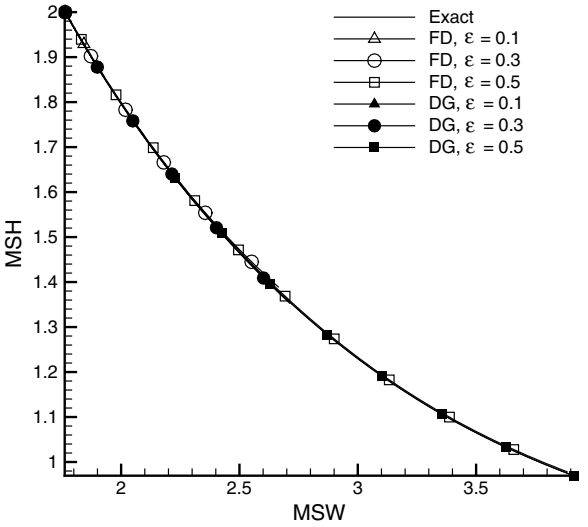

Fig. 9. Correlation between MSH and MSW obtained by the DG/PC and FD/PC methods, for time up to $t = 1$ ($A = 1$).

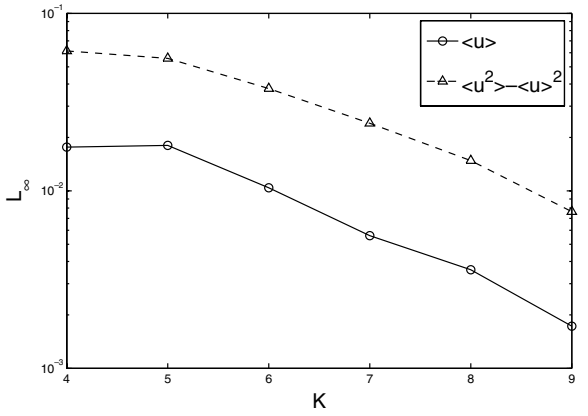

Fig. 10. DG method: convergence rate of L_∞-error of the *mean*, and *variance* in solving Eq. (2) with ($\epsilon = 0.3$), at $t = 1$, with respect to PC order, K.

2.3. Discussion

2.3.1. Color noise versus white noise

Consider the time-dependent random noise described in Eq. (13). The second moment of $W(\xi, t)$ (Eq. (3)) is

$$\langle W^2(\xi,t)\rangle = \epsilon^2 \int_0^{t_1}\int_0^{t_2} \langle \eta(\xi,t_1),\eta(\xi,t_2)\rangle \, \mathrm{d}t_1 \, \mathrm{d}t_2 = \epsilon^2 \int_0^{t_1}\int_0^{t_2} \mathrm{e}^{-\frac{|t_1-t_2|}{A}} \, \mathrm{d}t_1 \, \mathrm{d}t_2. \tag{20}$$

We consider two limiting cases:

(1) If $A \to \infty$, $\eta(\boldsymbol{\xi}, t)$ approaches a random variable with zero mean and unit variance. Thus, $W(\xi, t) = \epsilon\eta t$, and

$$\langle W^2(\xi,t)\rangle = \epsilon^2\langle\eta^2\rangle t^2 = \epsilon^2 t^2 \propto t^2. \tag{21}$$

(2) If $A \to 0$, $\eta(\boldsymbol{\xi}, t)$ describes white noise, with $\langle\eta(\boldsymbol{\xi}, t)\rangle = 0$ and $\langle\epsilon\eta(\boldsymbol{\xi}, t_1), \epsilon\eta(\boldsymbol{\xi}, t_2)\rangle = 2\epsilon'\delta(t_1 - t_2)$. The corresponding relations for $W(\xi, t)$ are

$$\begin{aligned}\langle W(\boldsymbol{\xi},t)\rangle &= \int_0^t \epsilon\langle\eta(\boldsymbol{\xi},t)\rangle\,\mathrm{d}t = 0,\\ \langle W^2(\boldsymbol{\xi},t)\rangle &= \int_0^t\int_0^t \langle\epsilon\eta(\boldsymbol{\xi},t_1),\epsilon\eta(\boldsymbol{\xi},t_2)\rangle\,\mathrm{d}t_1\,\mathrm{d}t_2 = 2\epsilon' t \propto t.\end{aligned} \tag{22}$$

From these two limiting cases, we see that any time-dependent random process, $\eta(\boldsymbol{\xi},t)$, with finite correlation length, A, ($A \neq 0$) has the following behavior:

(1) At early time ($\frac{t}{A} \ll 1$), $\langle W^2(\xi,t)\rangle$ is proportional to t^2. After a transition region, it switches to linear growth at later time ($\frac{t}{A} \gg 1$).
(2) As the correlation length, A, increases, the transition from quadratic to linear time dependence is delayed. Therefore, overall $\langle W^2(\xi,t)\rangle$ grows faster with time.

In order to 'fairly' compare the effect of time-dependent additive *white* noise and *color* noise, we impose the following condition: the integral of white noise's covariance kernel,

$$\int_{-\infty}^{\infty}\langle\epsilon\eta(t_1),\epsilon\eta(t_2)\rangle\,\mathrm{d}(t_1-t_2) = 2\epsilon'\int_{-\infty}^{\infty}\delta(t_1-t_2)\,\mathrm{d}(t_1-t_2) = 2\epsilon', \tag{23}$$

be equal to the integral of the random process's exponential kernel,

$$\int_{-\infty}^{\infty}\langle\epsilon\eta(t_1),\epsilon\eta(t_2)\rangle\,\mathrm{d}(t_1-t_2) = \int_{-\infty}^{\infty}\epsilon^2\mathrm{e}^{-\frac{|t_1-t_2|}{A}}\,\mathrm{d}(t_1-t_2) = 2\epsilon^2 A. \tag{24}$$

Therefore, to compare the effect of time-dependent additive white noise and color noise, we need to maintain the following relation:

$$\epsilon = \sqrt{\frac{\epsilon'}{A}}. \tag{25}$$

From Eq. (25), we can see that as the correlation length $A \to 0$, and correspondingly amplitude $\epsilon \to \infty$, the color noise approaches the white noise. Fig. 11 shows the MSH as a function of time for different types of time-dependent additive noise, described as: random variable, random process (i.e., color noise with fixed correlation length, $A = 10, 1, 0.1, 0.01$), and white noise ($\epsilon' = 1$). For a consistent comparison, we vary A and ϵ of the color noise so that $\epsilon^2 A = \epsilon' = 1$. We observe a very strong dependence between the decay of MSH and the correlation length. For $A = 0.01$, the results are very close to the white noise results. In Fig. 12, we plot MSH as a function of time for different time-dependent random noise, described as random processes with correlation length, $A = 0.1$, 1 and 10, amplitude value $\epsilon = 0.3$, and white noise with $\epsilon' = 0.009$, 0.09 and 0.9 (obtained

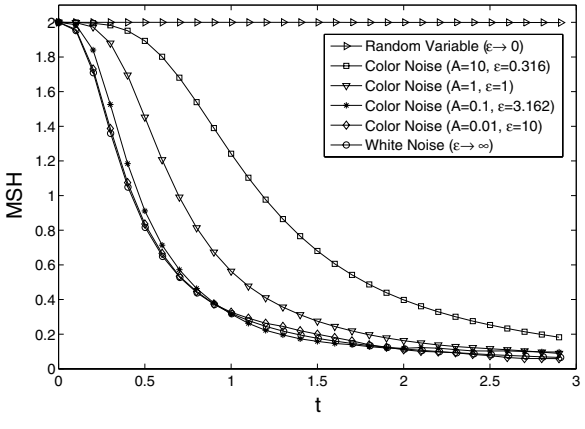

Fig. 11. MSH as a function of time. Time-dependent random noise, described as random variable, random process with correlation length, $A = 10$, 1, 0.1, 0.01 and white noise with $\epsilon' = 1$.

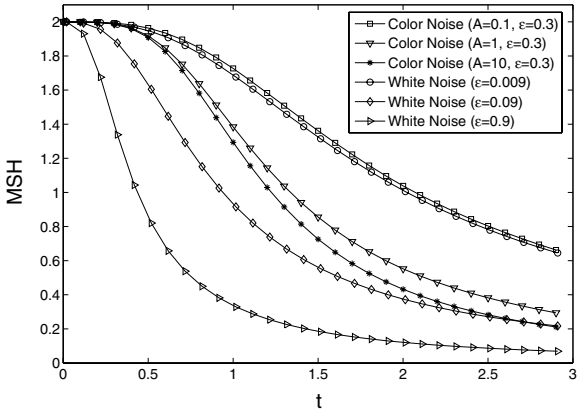

Fig. 12. MSH as a function of time. Time-dependent random noise, described as random process with correlation length $A = 0.1$, 1, 10, amplitude values $\epsilon = 0.3$, and white noise with $\epsilon' = 0.009$, 0.09 and 0.9.

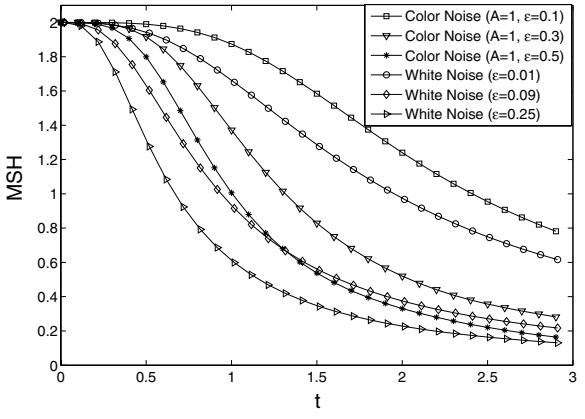

Fig. 13. MSH as a function of time. Time-dependent random noise, described as random process with correlation length $A = 1$, amplitude values $\epsilon = 0.1$, 0.3, 0.5, and white noise with $\epsilon' = 0.01$, 0.09 and 0.25.

from Eq. (25)). Fig. 12 shows that the color noise solutions approach the corresponding white noise solutions, as we decrease the correlation length A for the same amplitude of the color noise ϵ ($\epsilon = \sqrt{\frac{\epsilon'}{A}} = 0.3$). When $A \to 0$, MSH in color noise case will overlap with the MSH in corresponding white noise case. Fig. 13 shows MSH as a function of time for different time-dependent random noise, described as a random process with correlation length $A = 1$, amplitude values $\epsilon = 0.1, 0.3, 0.5$, and white noise with $\epsilon' = 0.01, 0.09$ and 0.25 (obtained from Eq. (25)). As we change the amplitude values of color noise and white noise ϵ and ϵ', respectively, and keep the same correlation length $A (A = \frac{\epsilon'}{\epsilon^2} = 1)$, an almost equal difference in MSH between color noise and corresponding white noise is observed.

2.3.2. Invariants for deterministic and stochastic KdV equation

Next, we investigate the effect of different space discretization methods on conservation properties. We computed the first, second, third and fourth invariants (I_1, I_2, I_3, I_4) of solution for the deterministic KdV equation.

$$I_1 = \int_\Omega u(x,t)\,\mathrm{d}x, \quad I_2 = \int_\Omega u^2(x,t)\,\mathrm{d}x,$$
$$I_3 = \int_\Omega \left[\frac{u^3(x,t)}{3} - \left(\frac{\partial u}{\partial x}\right)^2\right]\mathrm{d}x, \quad I_4 = \int_\Omega \left[\frac{u^4}{4} + \frac{9}{5}\left(\frac{\partial^2 u}{\partial x^2}\right)^2 - 3u\left(\frac{\partial u}{\partial x}\right)^2\right]\mathrm{d}x. \tag{26}$$

In Fig. 14, we present the error of the four invariants obtained by the DG and the FD methods. Higher accuracy is observed using the DG method, compared to the FD method.

For the stochastic KdV equation with time-dependent noise (Eq. (2)), the mean of the first invariant, $\langle I_1(\xi,t)\rangle$, can be obtained using the exact one-soliton solution, (Eq. (6)), as follows:

$$\begin{aligned}\langle I_1(\xi,t)\rangle &= \left\langle \int_\Omega u(\boldsymbol{\xi},x,t)\,\mathrm{d}x \right\rangle = \left\langle \int_\Omega W(\boldsymbol{\xi},t) - 2\kappa^2\mathrm{sech}^2\left\{\kappa(x-ct)+6\kappa\int_0^t W(\boldsymbol{\xi},t')\,\mathrm{d}t'\right\}\,\mathrm{d}x\right\rangle \\ &= \left\langle \int_\Omega W(\boldsymbol{\xi},t)\,\mathrm{d}x\right\rangle - \left\langle \int_\Omega 2\kappa^2\mathrm{sech}^2\left\{\kappa(x-ct)+6\kappa\int_0^t W(\boldsymbol{\xi},t')\,\mathrm{d}t'\right\}\,\mathrm{d}x\right\rangle. \end{aligned} \tag{27}$$

Since $\int_\Omega \mathrm{sech}^2\{\kappa(x-ct)+6\kappa\int_0^t W(\boldsymbol{\xi},t')\,\mathrm{d}t'\}\,\mathrm{d}x = \int_\Omega \mathrm{sech}^2\{\kappa(x-ct)\}\,\mathrm{d}x = -4\kappa$, we have,

$$-\left\langle \int_\Omega 2\kappa^2\mathrm{sech}^2\left\{\kappa(x-ct)+6\kappa\int_0^t W(\boldsymbol{\xi},t')\,\mathrm{d}t'\right\}\,\mathrm{d}x\right\rangle = -4\kappa. \tag{28}$$

For any time-dependent random perturbation with zero mean, we always have

$$\left\langle \int_\Omega W(\xi,t)\,\mathrm{d}x\right\rangle = \int_\Omega\int_0^t \epsilon\langle\eta(\xi,t)\rangle\,\mathrm{d}t\,\mathrm{d}x = 0. \tag{29}$$

Therefore, for the stochastic KdV equation perturbed by time-dependent noise with zero mean (Eq. (2)), the mean of the first invariant, $\langle I_1(\xi,t)\rangle$, is constant and equal to the deterministic case, i.e.,

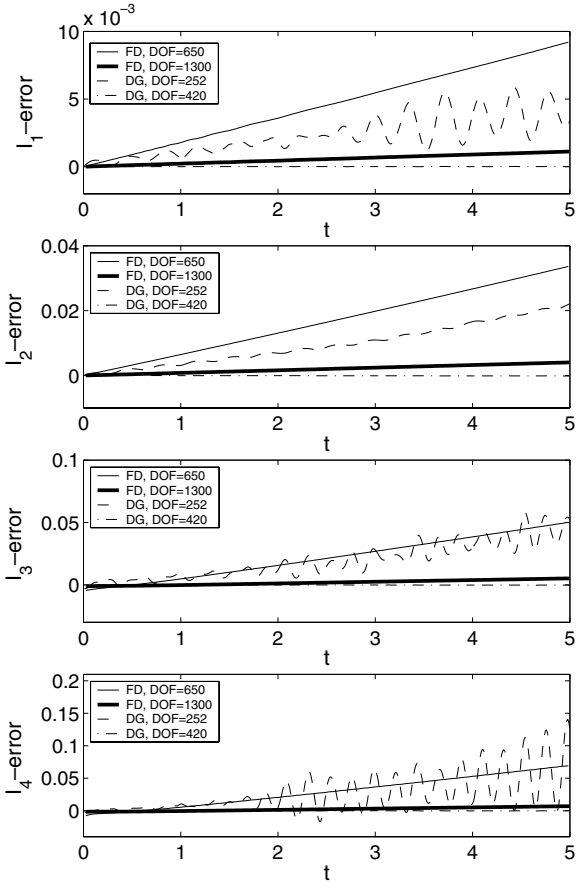

Fig. 14. Error of the first, second, third and fourth invariants, Eq. (26), for the deterministic KdV equation, where the relative error is defined as $\frac{|I_{\text{exact}}-I_{\text{num}}|}{|I_{\text{exact}}|}$.

$$\langle I_1(\xi,t)\rangle = -4\kappa = I_1. \tag{30}$$

Similarly, $\langle I_2(\xi,t)\rangle$ can be obtained from:

$$\begin{aligned}\langle I_2(\xi,t)\rangle &= \left\langle \int_\Omega u^2(\boldsymbol{\xi},x,t)\,\mathrm{d}x \right\rangle = \left\langle \int_\Omega \left\{ W(\boldsymbol{\xi},t) - 2\kappa^2 \mathrm{sech}^2\left(\kappa(x-ct) + 6\kappa\int_0^t W(\boldsymbol{\xi},t')\,\mathrm{d}t'\right)\right\}^2 \mathrm{d}x \right\rangle \\ &= \left\langle \int_\Omega W^2(\boldsymbol{\xi},t)\,\mathrm{d}x \right\rangle - 4\left\langle \int_\Omega W(\boldsymbol{\xi},t)\kappa^2 \mathrm{sech}^2\left\{\kappa(x-ct) + 6\kappa\int_0^t W(\boldsymbol{\xi},t')\,\mathrm{d}t'\right\}\mathrm{d}x\right\rangle \\ &\quad + 4\left\langle \int_\Omega \kappa^4 \mathrm{sech}^4\left\{\kappa(x-ct) + 6\kappa\int_0^t W(\boldsymbol{\xi},t')\,\mathrm{d}t'\right\}\mathrm{d}x\right\rangle. \end{aligned} \tag{31}$$

Since $\int_\Omega \mathrm{sech}^2\{\kappa(x-ct) + 6\kappa\int_0^t W(\boldsymbol{\xi},t')\,\mathrm{d}t'\}\,\mathrm{d}x = \int_\Omega \mathrm{sech}^2\{\kappa(x-ct)\}\,\mathrm{d}x = -4\kappa$, we have

$$\begin{aligned} &-4\left\langle \int_\Omega W(\boldsymbol{\xi},t)\kappa^2 \mathrm{sech}^2\left\{\kappa(x-ct) + 6\kappa\int_0^t W(\boldsymbol{\xi},t')\,\mathrm{d}t'\right\}\mathrm{d}x\right\rangle \\ &= -4\left\langle W(\boldsymbol{\xi},t)\int_\Omega \kappa^2 \mathrm{sech}^2\left\{\kappa(x-ct) + 6\kappa\int_0^t W(\boldsymbol{\xi},t')\,\mathrm{d}t'\right\}\mathrm{d}x\right\rangle \\ &= -4\left\langle W(\boldsymbol{\xi},t)\int_\Omega \kappa^2 \mathrm{sech}^2(\{\kappa(x-ct)\})\,\mathrm{d}x\right\rangle = -4\int_\Omega \kappa^2 \mathrm{sech}^2\{\kappa(x-ct)\}\,\mathrm{d}x\langle W(\boldsymbol{\xi},t)\rangle = 0. \end{aligned} \tag{32}$$

Similarly,

$$4\left\langle \int_\Omega \kappa^4 \mathrm{sech}^4\left\{\kappa(x-ct) + 6\kappa\int_0^t W(\boldsymbol{\xi},t')\,\mathrm{d}t'\right\}\mathrm{d}x\right\rangle = 4\int_\Omega \kappa^4 \mathrm{sech}^4(\kappa(x-ct))\,\mathrm{d}x = I_2. \tag{33}$$

Thus, for the stochastic KdV equation with time-dependent noise (Eq. (2)), $\langle I_2(\xi,t)\rangle$ is growing with time, as follows:

$$\langle I_2(\xi,t)\rangle = I_2 + \langle W^2(\boldsymbol{\xi},t)\rangle \int_\Omega \mathrm{d}x, \tag{34}$$

where I_2 is the deterministic second invariant. For example, for the stochastic KdV equation perturbed by random noise, described as a *random variable*, $\langle I_2(\xi,t)\rangle$ can be expressed as

$$\langle I_2(\xi,t)\rangle = I_2 + \epsilon^2 t^2 \int_\Omega \mathrm{d}x. \tag{35}$$

For the stochastic KdV equation perturbed by time-dependent noise, described as a *random process*, $\langle I_2(\xi,t)\rangle$ can be expressed as

$$\langle I_2(\xi,t)\rangle = I_2 + \epsilon^2 \int_0^{t_1}\int_0^{t_2} \mathrm{e}^{-\frac{|t_1-t_2|}{A}}\,\mathrm{d}t_1\,\mathrm{d}t_2 \int_\Omega \mathrm{d}x. \tag{36}$$

For the stochastic KdV equation perturbed by time-dependent noise, described as a *white noise*, $\langle I_2(\xi,t)\rangle$ can be expressed as

$$\langle I_2(\xi,t)\rangle = I_2 + 2\epsilon' t \int_\Omega \mathrm{d}x. \tag{37}$$

Fig. 15 shows $\langle I_2(\xi,t)\rangle$, for the stochastic KdV equation with time-dependent noise (Eq. (2)), described as a random variable and as a random process with correlation length, $A = 10$, 1 and 0.1. For the stochastic KdV equation with time-dependent noise (Eq. (2)), described as a random process, $\eta(\boldsymbol{\xi},t)$, with finite correlation length, A ($A \neq 0$), $\langle I_2(\xi,t)\rangle$ has the following behavior:

(1) At early time ($\frac{t}{A} \ll 1$), $\langle I_2(\xi,t)\rangle$ is proportional to t^2. After a transition period, it switches to linear growth at later time ($\frac{t}{A} \gg 1$).
(2) As the correlation length, A, increases, the transition from quadratic to linear time dependence is delayed. Therefore, overall $\langle I_2(\xi,t)\rangle$ grows faster with time.

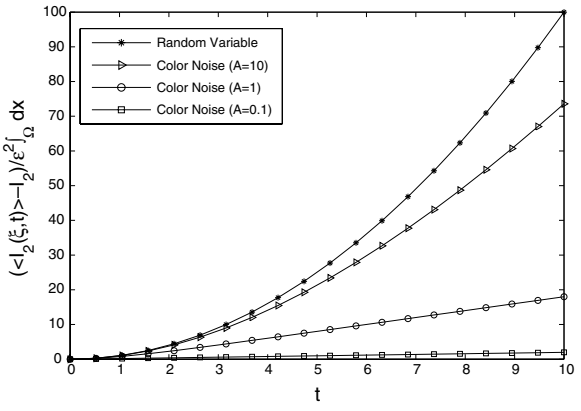

Fig. 15. The mean of the second invariant, $\langle I_2(\xi,t)\rangle$, for the stochastic KdV equation with time-dependent noise (Eq. (2)), described as a random variable, random process with correlation length $A = 10$, 1 and 0.1.

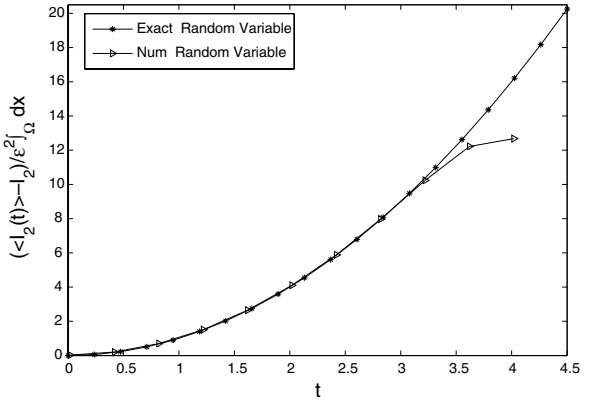

Fig. 16. Exact and numerical mean solution of the second invariant, $\langle I_2(\xi,t)\rangle$, for the stochastic KdV equation with time-dependent noise (Eq. (2)), described as a random variable. The polynomial chaos solution breaks down after time $t \geqslant 3$.

Fig. 16 shows the exact and numerical mean of the second invariant, $\langle I_2(\xi,t)\rangle$, for the stochastic KdV equation with time-dependent noise (Eq. (2)), described as a random variable. The numerical solution is obtained by the DG/PC method with eighth-order PC expansions. The deviation of the numerical solution from the exact one at later time shows a breakdown of the polynomial chaos approach for long-time integration. This has been observed before, e.g. [26], and can be fixed by discretizing the random variable using a multi-element approach, e.g., see [27].

2.3.3. Gaussian packet

The one-soliton solution of the deterministic KdV equation can be described as a soliton moving with a constant speed, and maintaining its initial shape. In contrast, in the stochastic case, the one-soliton mean solution can be described as a soliton moving with a constant speed, but changing shape from $\mathrm{sech}^2(x)$ to a Gaussian packet, $g(x,t) \sim \exp(-(x-ct)^2/a)$. The area, enclosed under the mean soliton, is the first invariant, I_1. Let us define a function, $g(x,t)$, as an approximating function to $\langle u(\xi,x,t)\rangle$ in the following manner:

$$g(x,t) = C_0(t)\mathrm{e}^{-(x-ct)^2/a}, \tag{38}$$

where $C_0(t)$ is an instantaneous soliton height, c is wave speed and a is computed from

$$\int_{-\infty}^{\infty} g(x,t)\,\mathrm{d}x = \int_{-\infty}^{\infty} \langle u(\xi,x,t)\rangle\,\mathrm{d}x.$$

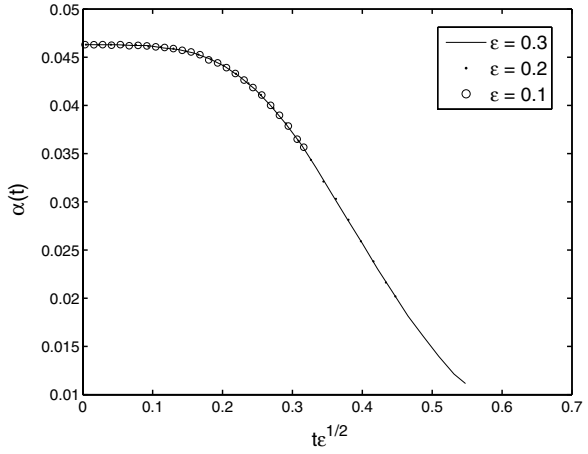

Fig. 17. Variation of $\alpha(t)$. The numerical solution obtained using one-dimensional eighth-order DG/PC method.

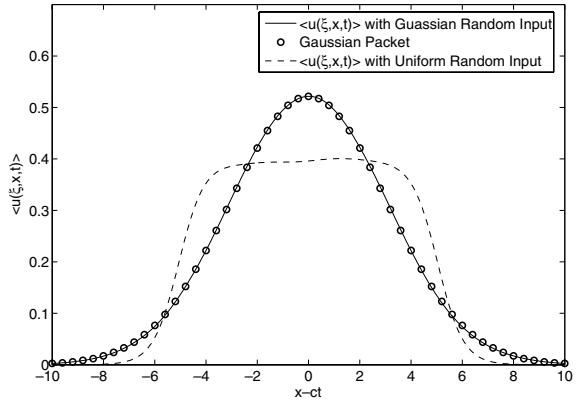

Fig. 18. One-soliton mean solution, $\langle u(\xi, x, t)\rangle$, at $t = 1.8$, as a function of x for Gaussian random variable, uniform random variable, and the Gaussian packet approximation for Gaussian random input.

The deviation from the Gaussian shape is described by $\alpha(t)$ which can be estimated from

$$\alpha(t) = \frac{1}{C_0(t)}\mathrm{MAX}_x(|\langle u(\xi, x, t)\rangle - g(x, t)|).$$

In Fig. 17, we present the variation of $\alpha(t)$. Using proper scaling, we show that $\langle u(\xi, x, t)\rangle$ approaches the Gaussian packet as $t\epsilon^{1/2}$ increases.

Thus, we have shown that under the Gaussian random perturbation, the shape of the mean soliton solution changes from $\mathrm{sech}^2(x)$ to a Gaussian packet. However, for the KdV equation subject to uniform random perturbation, the mean soliton solution changes its basic shape from $\mathrm{sech}^2(x)$ to a uniform-like packet. Fig. 18 shows the one-soliton mean solutions, $\langle u(\xi, x, t)\rangle$, at $t = 1.8$ for Gaussian random variable and uniform random variable as inputs. The one-soliton mean solution with Gaussian random perturbation becomes a Gaussian packet eventually. However, the one-soliton mean solution with uniform random perturbation has not converged to a Gaussian packet for the same time integration.

3. Space-dependent multiplicative noise

We now consider the second study case, where we include the stochastic input in the KdV as space-dependent multiplicative noise. Specifically, by setting $\epsilon = 0$ in Eq. (1), we obtain

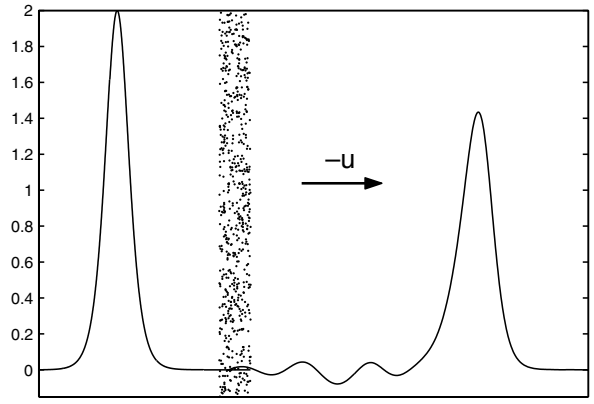

Fig. 19. Sketch of a soliton wave passing through the random medium.

$$\begin{aligned} &u_t + (-6u + v\zeta(\xi, x))u_x + u_{xxx} = 0, \quad x \in (-\infty, \infty), \\ &u(\zeta = 0, x, t = 0) = -2\kappa^2 \mathrm{sech}^2(\kappa x). \end{aligned} \tag{39}$$

We consider the case where the soliton passes through a small random subregion of the domain. As we will show in the following, after the soliton passes through this random strip it leaves behind small ripples due to dispersion and its overall shape changes, see Fig. 1(b).

Fig. 19 is a sketch of a soliton wave passing through the random medium, located in the strip $x \in [1.5, 3.5]$. We set the computational domain to be $x \in [-10, 20]$ and we integrate the KdV equation up to time $t = 1.5$. In the following, we will first consider the stochastic input as a random *variable* and subsequently as a random *process*.

3.1. Fully-correlated Gaussian noise

The fully-correlated random noise ζ can be described as a random variable ξ, and Eq. (1) is simplified to

$$\begin{aligned} &u_t + (-6u + v\xi)u_x + u_{xxx} = 0, \quad x \in (-\infty, \infty), \\ &u(\zeta = 0, x, t = 0) = -2\kappa^2 \mathrm{sech}^2(\kappa x). \end{aligned} \tag{40}$$

In Fig. 20, we plot the mean and variance of the solution $u(\xi, x, t)$ for Eq. (40). Increasing the amplitude, v, leads to a faster decay of the soliton. Moreover, the soliton moves slower and larger dispersive waves are observed behind the soliton. For this simulation we employed eighth-order Hermite polynomials for the PC expansion while for the DG discretization we used 30 spectral elements of seventh-order. Figs. 21(a) and (b) show numerical results for the height MSH and the width MSW, respectively, as a function of time. We have also included results obtained with Monte Carlo simulations (2000 runs) based on the FD discretization with 1200 grid points as well as results from a FD/PC simulation. In this case we do not have an exact solution, but the agreement with the Monte Carlo simulation is very good except at the large amplitude $v = 0.5$ at later times. Increasing the amplitude v of the random noise leads to lower values of MSH and higher values of MSW as time increases.

3.2. Partially-correlated Gaussian noise

Here we treat $\zeta(\xi, x)$ as a space-dependent random process, described as a second-order autoregressive process; see details in [28]:

$$\begin{aligned} &\zeta_i = \frac{b}{2}(\zeta_{i-1} + \zeta_{i+1}) + a\xi_i, \quad i = 1, 2, \ldots, N, \\ &b = \mathrm{e}^{-\frac{\Delta x^2}{2A^2}}, \quad a = -0.5(\Delta x)^{\frac{3}{2}}\mathrm{e}^{-\frac{\Delta x^2}{2A^2}}, \end{aligned} \tag{41}$$

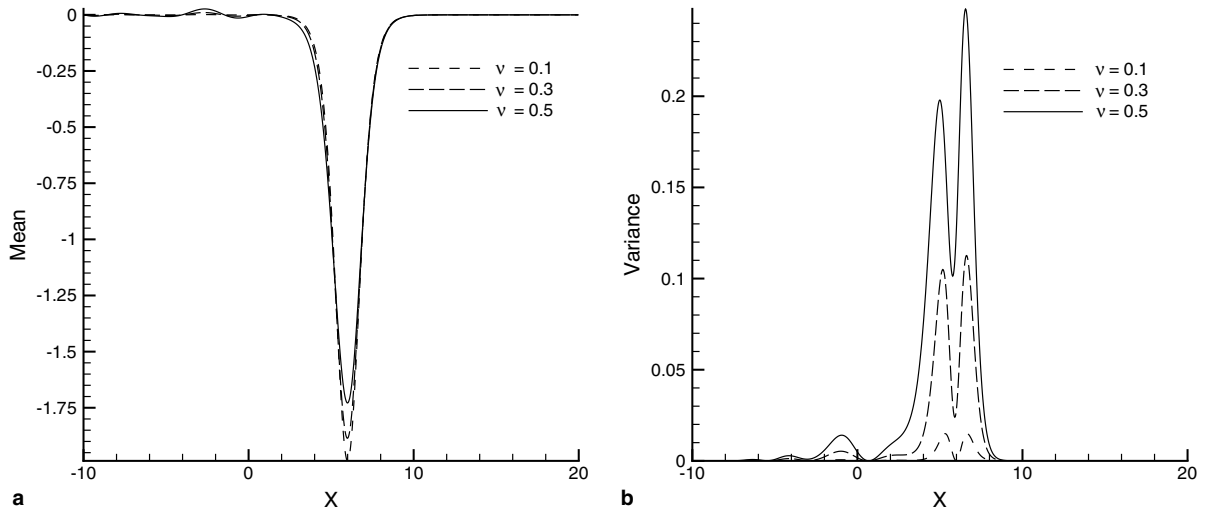

Fig. 20. Random variable case: (a) mean and (b) variance of $u(\xi, x, t)$ obtained by the DG/PC method at $t = 1.5$, after the soliton passes through the random medium $x \in [1.5, 3.5]$. Three simulations are shown at amplitude $v = 0.1$, 0.3 and 0.5.

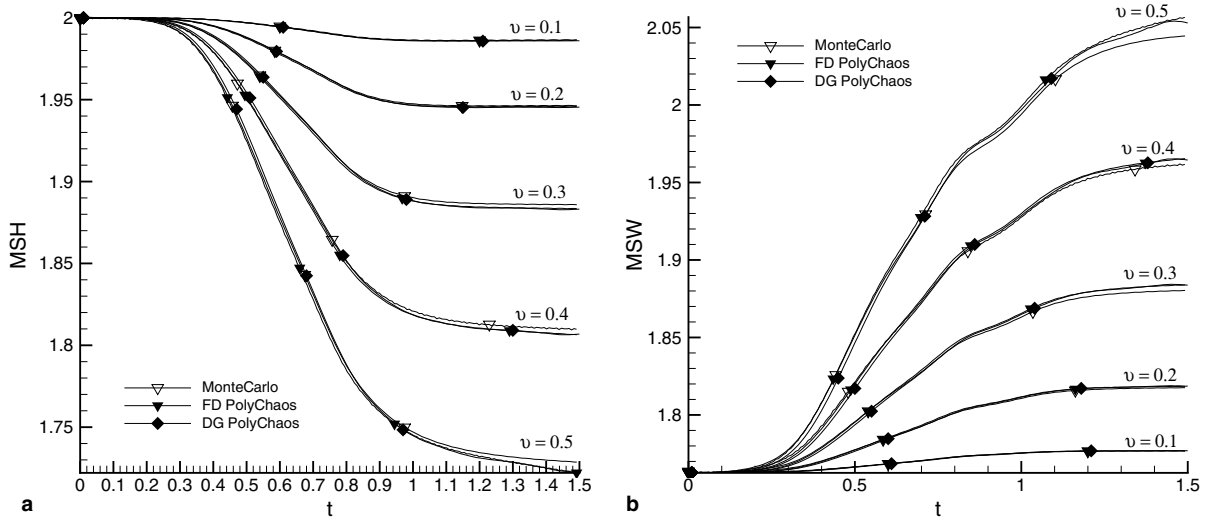

Fig. 21. Random variable case: (a) mean soliton height (MSH) and (b) mean soliton width (MSW) versus time for amplitude values $v = 0.1$, 0.2, 0.3, 0.4 and 0.5.

where A is the correlation length in space. The non-stationary covariance of the above process is given by:[1]

$$\begin{aligned}\langle \zeta(x), \zeta(y) \rangle = \frac{1}{8k^3 \sinh^2(kL)} & (\sinh(k(|y-x|)) - \sinh(k(x+y)) + \sinh(k(x+y-2L)) \\ & - \sinh(k(|y-x|-2L)) + k(x+y-2L)\cosh(k(x+y)) - k(x+y)\cosh(k(x+y-2L)) \\ & + k(2L-|y-x|)\cosh(k(y-x)) + k|y-x|\cosh(k(|y-x|-2L))), \end{aligned} \tag{42}$$

[1] This formula was obtained by Prof. C.-H. Su at Brown University.

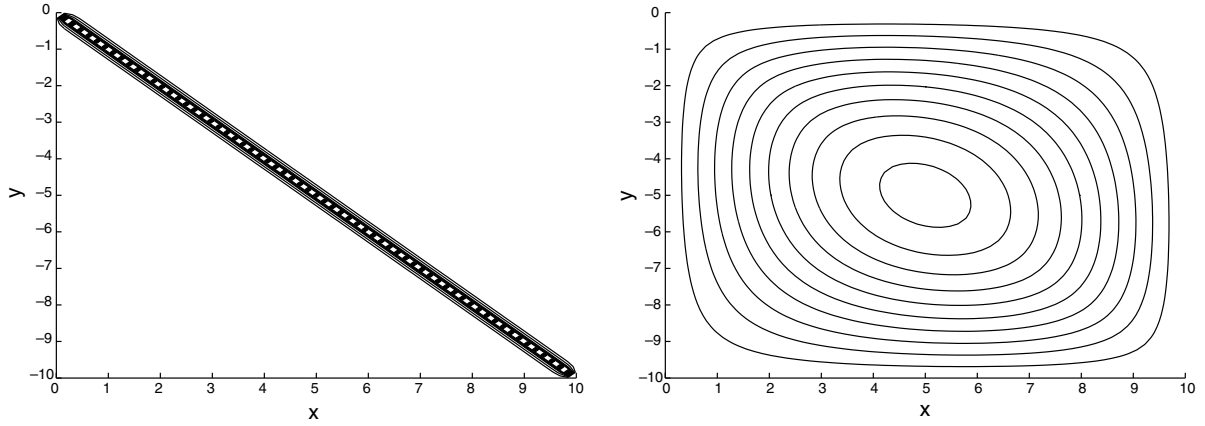

Fig. 22. Space-dependent covariance kernel for the the random medium. Left: correlation length $A/L = 0.01$; Right: correlation length $A/L = 100$.

where $k = \frac{1}{A}$ and L is the length of the space-dependent random medium. Fig. 22 shows the numerically generated space-dependent covariance kernel for $A/L = 0.01$ and 100. We can see, for $A/L = 0.01$, the covariance kernel is centered along the cross-diagonal while for $A/L = 100$, the covariance kernel is quite uniform.

Fig. 23 shows the mean and variance of the solution at a fixed time $t = 1.5$ for different values of the noise amplitude. The mean solution exhibits large oscillations trailing the solition, which are characteristic of dispersion waves. The wave speed of these small dispersive waves is small compared to the wave speed of the soliton. There is no phase shift on the right side of the soliton. We note that by increasing the amplitude of the random noise, a faster decay of the soliton is observed as a function of time. Fig. 1(b) (see Section 1) shows a three-dimensional view of the mean stochastic solitons at different times for $L = 2$, $A/L = 1$ and amplitude $v = 6$. We can see in this view small ripples formed behind the soliton while the MSH drops as the soliton passes through the random medium. However, after the soliton leaves the random medium the value of MSH stays constant. These solutions were obtained with the DG/PC method, with 30 spectral elements of variable p-order; for the stochastic approximation $N = 3$ Karhunen–Loeve expansions and sixth-order Hermite polynomials were employed. Fig. 24 shows the mean and variance of $u(\xi, x, t)$ after passing through

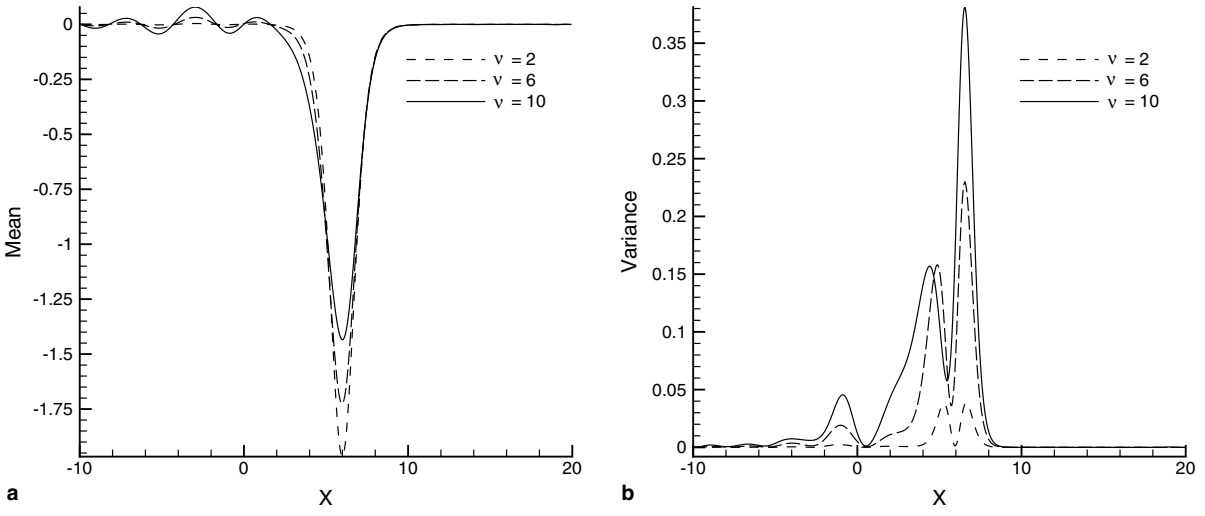

Fig. 23. Mean (a) and variance (b) of $u(\xi, x, t)$ at $t = 1.5$ obtained by the DG/PC method, after the soliton has passed through the random medium; $L = 2$, $A/L = 1$, amplitude $v = 2$, 6 and 10.

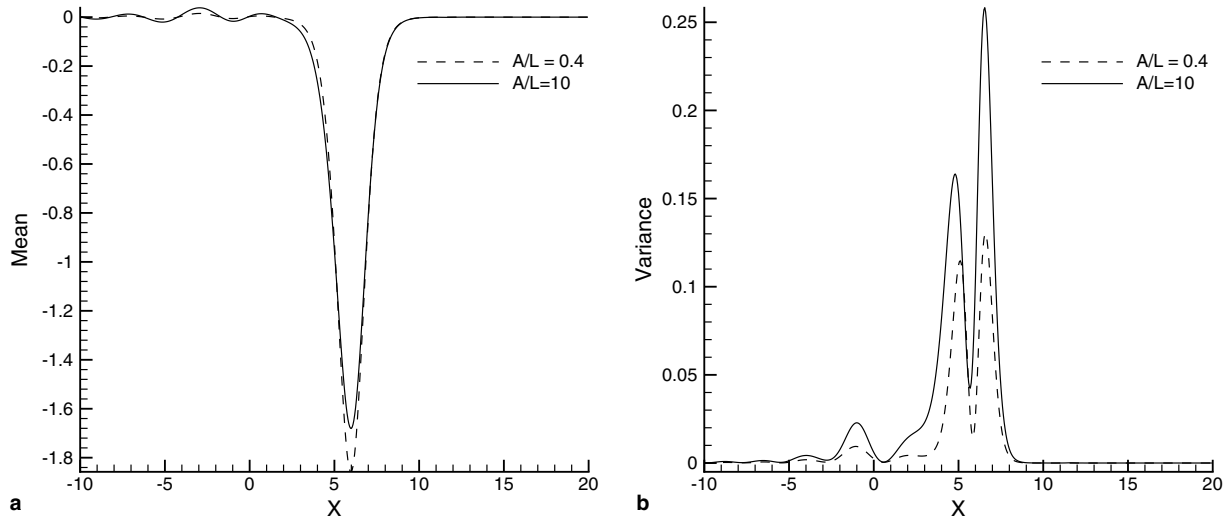

Fig. 24. Mean (a) and variance (b) of $u(\xi, x, t)$ obtained by the DG/PC method, after the soliton has passed through the random medium; $L = 2$, $A/L = 0.4$ and 10, amplitude $v = 6$, time $t = 1.5$.

the random medium for a covariance kernel corresponding to $L = 2$, $A/L = 0.4$ and 10, and amplitude values $v = 6$, at $t = 1.5$. By increasing the correlation length of the random process a faster drop of the soliton and larger dispersive waves for increasing time are observed. Figs. 25(a) and (b) show numerical results obtained by the DG/PC and FD/PC methods and by Monte Carlo simulations; the latter is based on 2000 runs using FD discretization on 1200 grid points. The polynomial chaos simulations are computed by a three-dimensional, third-order polynomial chaos method. In spatial discretization, a DG method with 30 spectral elements of sixth-order and a second-order FD method with 1200 grid points are used. MSH and MSW are plotted as a function of time for relatively large values of the noise amplitude. We see that for the largest value ($v = 10$) we have a deviation of the PC-based results from the Monte Carlo results. In Figs. 26(a) and (b), we plot MSH and MSW as a function of time for different correlation lengths along with Monte Carlo results. Surpisingly,

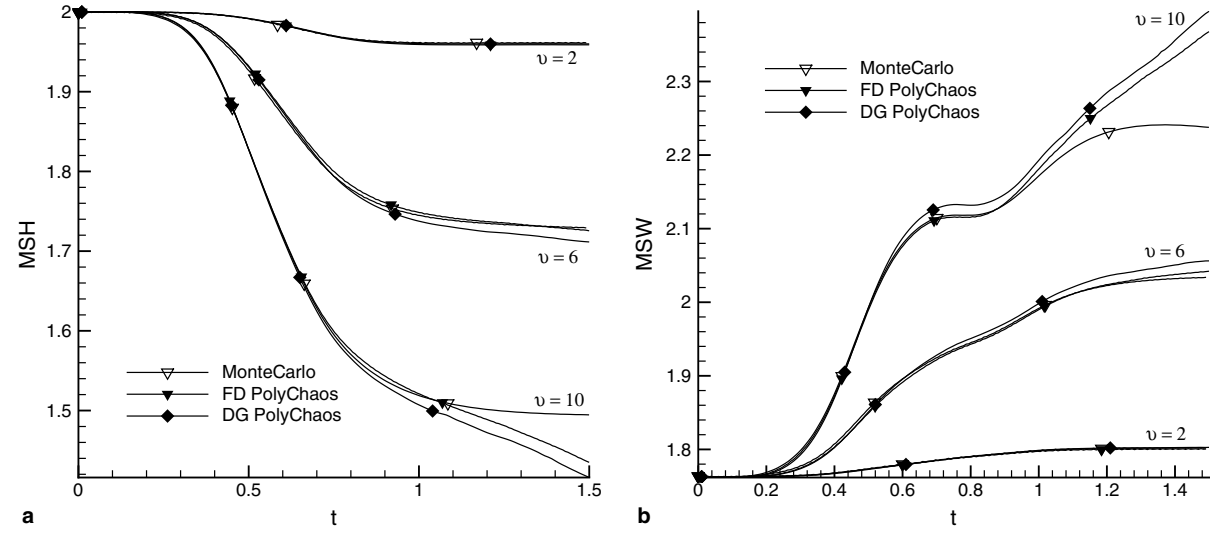

Fig. 25. MSH (a) and MSW (b) as a function of time while the soliton is passing through the random medium; $L = 2$, $A/L = 1$, amplitude values $v = 2$, 6 and 10.

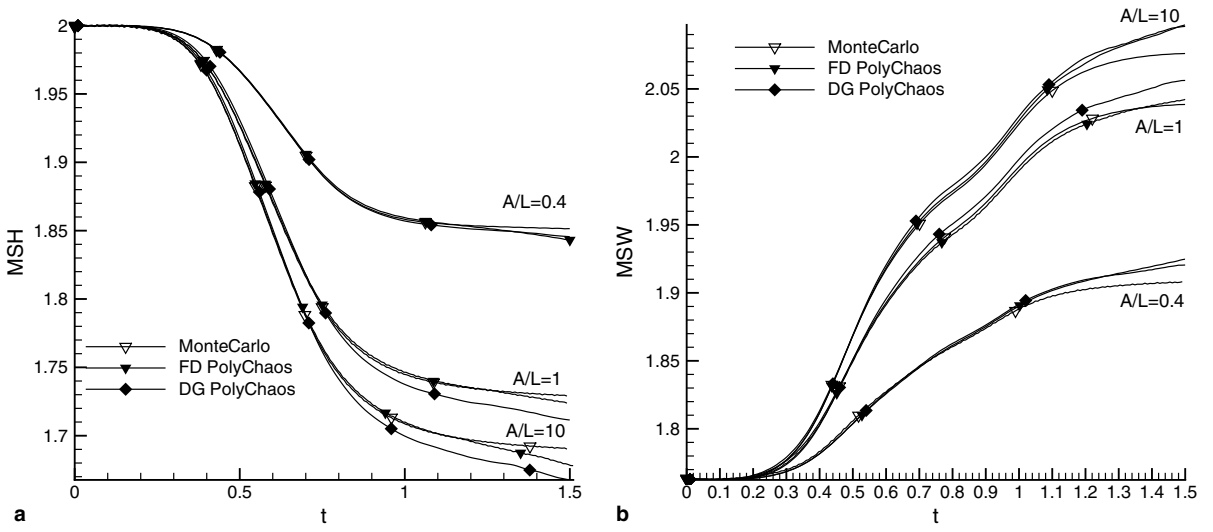

Fig. 26. MSH (a) and MSW (b) as a function of time while the soliton passing through the random medium; $L = 2$, amplitude $v = 6$, correlation length values $A/L = 0.4$, 1 and 10.

here we see deviations of the PC based results from the Monte Carlo simulations at larger values of the correlation length. The FD/PC results are closer with the Monte Carlo simulations since we employed FD discretization in both approaches. Increasing the A/L ratio leads to fast decay of MSH, which is a trend consistent with the results obtained with the fully-correlated noise case.

We have also investigated the convergence rate for this case. In Fig. 27, we plot the L_∞ error in the mean solution and the variance at $t = 1$ for space-dependent noise with correlation length $A/L = 1$ and amplitude $v = 6$. The number of Karhunen–Loeve modes is $N = 2$ and high-order spatial and temporal discretization is employed to guarantee the stochastic error dominates. (We use DG discretization with 180 DOF in space and $\Delta t = 10^{-5}$ in time). The L_∞ error for the mean and the variance are defined in Eq. (19). Since there is no analytical solution for space-dependent noise, we treat the numerical mean and variance solutions obtained for $K = 9$ as the exact mean and variance solutions. Similar exponential convergence rates are observed for both mean and variance in the semi-log plot.

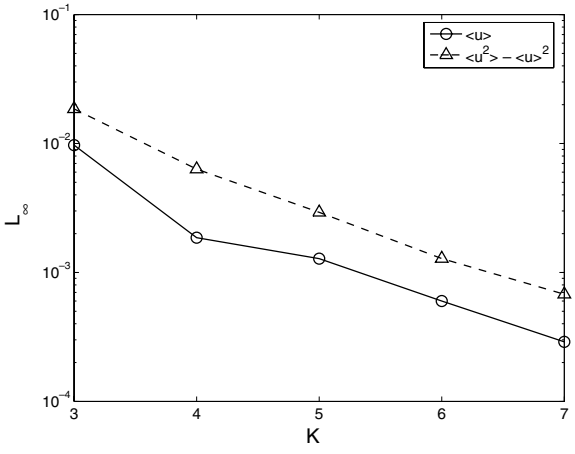

Fig. 27. DG method: convergence rate of L_∞-error of the *mean*, and *variance* in solving Eq. (39) with ($v = 6$, $\epsilon = 0$, $A/L = 1$), at $t = 1$, with respect to PC order, K.

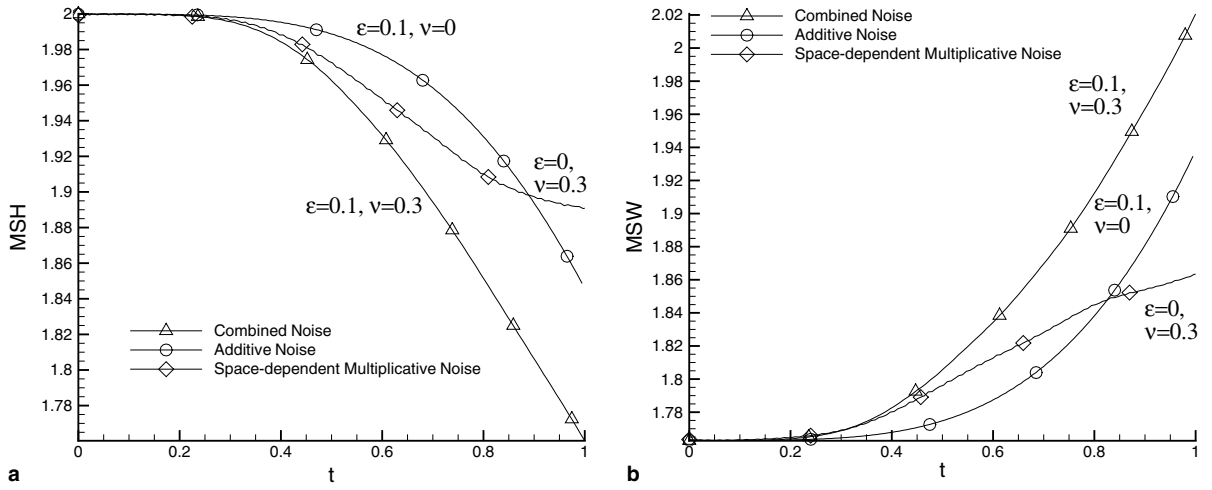

Fig. 28. MSH (a) and MSW (b) as a function of time while the soliton under additive noise, described as a random variable ($\epsilon = 0.1$) passing through a random medium corresponding to $L = 2$, amplitude $v = 0.3$.

4. Additive noise and space-dependent multiplicative noise

We now consider the third case, where we include the stochastic input in the KdV as space-dependent multiplicative noise and also additive noise, see Eq. (1). In Fig. 28, we plot the MSH and MSW for this combined case. We compare the solution with corresponding solutions obtained for an additive noise and a space-dependent multiplicative noise with the same values of parameters. We observed that the combined noise case leads to a faster decay in MSH and a faster increase in MSW.

5. Summary

We have obtained numerical solutions of the stochastic Korteweg-de Vries equation, an idealized model for noisy plasmas. First, we considered time-dependent additive noise for which exact solutions are available in the literature. Subsequently, we considered multiplicative space-dependent noise corresponding to a new non-stationary covariance kernel. Finally, we studied the combined case. The first two classes of solutions are very different as shown in Fig. 1 (see Section 1) in terms of their mean values. The dominant feature of the mean stochastic solution in the first class is the fast decay of the soliton height whereas in the second class is the presence of ripples trailing the soliton as it passes through a "noisy" medium. We have also obtained several other useful and general results for the time-dependent case. For example, if the additive noise is of Gaussian type then the solution converges to a Gaussian packet whereas if the input noise follows a uniform distribution then the solution follows a "uniform-like" distribution with short tails – at least for early to modest travelling times. We have also found that the mean first invariant is constant and its value is identical to the deterministic value whereas the second invariant increases quadratically with time at early times but switches to linear growth eventually.

From the numerical standpoint, this problem is a good testbed for measuring the accuracy of new stochastic numerical solvers. Here we focused on polynomial chaos (PC), using Hermite and Legendre basis functionals. We also employed two different discretizations in physical space, a spectral/hp element combined with a discontinuous Galerkin (DG) method and a second-order finite difference (FD) method. Overall, the accuracy of PC with either discretization is very good at early times or well correlated input, and only a few modes were required to achieve very high accuracy (e.g., see Figs. 4, 10 and 27). However, in long-time integration, the PC-based solutions obtained by either DG or FD discretization diverge (see Fig. 16), a behavior not entirely unexpected, e.g. see [26]. To this end, a multi-element discretization of random space with adaptive control of the error can overcome this problem. First results for time-dependent problems were reported in [27], and we will report more details in future publications.

Acknowledgments

This work was supported by the Computational Mathematics Program of AFOSR. Computations were performed at NCSA, NPACI and PSC.

Appendix A. Numerical methods

We perform two types of stochastic simulations. One is based on the Monte Carlo method and the other one is based on the polynomial chaos method. In Monte Carlo and polynomial chaos simulations, the representation of *stochastic inputs* is expressed by a Karhunen–Loeve decomposition.

In polynomial chaos representation, we employ Wiener–Hermite expansions for the solution in the form

$$u(\xi, x, t) = \sum_{i=0}^{M} u_i(x, t)\phi_i(\xi), \tag{43}$$

where $\{\phi_i\}$ is the expansion basis. We choose $\{\phi_i\}$ to be the normalized Hermite polynomials of degree K. Here ξ is a N-dimensional Gaussian random vector. The total number of expansion terms is $(M+1)$, and is determined by the dimensions N of the random vector ξ and the highest order K of the polynomials $\{\phi_i\}$,

$$M + 1 = \frac{(N+K)!}{(N!K!)}. \tag{44}$$

The most important aspect of the above chaos expansion is that the random processes have been decomposed into a set of deterministic functions (in spatial–temporal variables) multiplied by the random basis polynomials which are independent of spatial–temporal variables. Substituting Eq. (43) into polynomial chaos representation (Eq. (1)) and letting $v = 0$, we obtain the stochastic KdV equation with time-dependent random noise

$$\sum_{i=0}^{M} \frac{\partial u_i \phi_i}{\partial t} - \frac{\partial}{\partial x}\left(3\sum_{i=0}^{M}\sum_{j=0}^{M} u_i u_j \phi_i \phi_j\right) + \sum_{i=0}^{M} \frac{\partial^3 u_i}{\partial x^3}\phi_i = \epsilon \sum_{i=0}^{M} \eta_i \phi_i. \tag{45}$$

By multiplying Eq. (45) by a test function, ϕ_k, $k = 0, \ldots, M$ and employing the orthogonality relation, We obtain a system of $(M+1)$ deterministic 'KdV-like' equations,

$$\frac{\partial u_k}{\partial t} - \frac{\partial}{\partial x}\left(\frac{3}{e_{0,k,k}}\sum_{i=0}^{M}\sum_{j=0}^{M} u_i u_j e_{i,j,k}\right) + \frac{\partial^3 u_k}{\partial x^3} = \epsilon\eta_k, \tag{46}$$

where $e_{0,k,k} = \langle \phi_k^2 \rangle$ and $e_{i,j,k} = \langle \phi_i \phi_j \phi_k \rangle$, $i, j, k = 0, \ldots, M$. Both $e_{0,k,k}$ and $e_{i,j,k}$ are evaluated during the pre-processing stage.

In space and time discretization, we employ two numerical techniques:

(1) A high-order discontinuous Galerkin (DG) method [24] with first-order predictor–corrector time stepping scheme.
(2) A second-order (in space) finite difference (FD) method [25] with first-order time stepping scheme.

According to the DG method, the computational domain, Ω, is decomposed into N_{el} non-overlapping sub-domains, $\Omega = \bigcup_{j=1}^{N_{\mathrm{el}}} \Omega_j$, $\Omega_j = \{x | x_{j-1/2} \leqslant x \leqslant x_{j+1/2}\}$. The differential equations are solved *independently* in each sub-domain, while the boundary conditions are specified on the interfaces between Ω_j and $\Omega_{j\pm1}$.

Eq. (46) is decomposed into three first order differential equations by introducing the auxiliary terms, q, p and r as following

$$q = \frac{\partial u_k}{\partial x}, \quad p = \frac{\partial q}{\partial x}, \quad r = \frac{\partial p}{\partial x}, \tag{47a}$$

$$\frac{\partial u_k}{\partial t} - \frac{\partial}{\partial x}\left(\frac{3}{e_{0,k,k}}\sum_{i=0}^{M}\sum_{j=0}^{M} u_i u_j e_{i,j,k}\right) + r = \epsilon\eta_k. \tag{47b}$$

By multiplying Eqs. (47a) and (47b) by a test function, $v_m(x)$, where $m = 0, 1, \ldots, P$ and $x \in \Omega_j$ and integrating by parts over the sub-domain Ω_j, we transform Eqs. (47a) and (47b) into a weak form:

$$\int_{\Omega_j} v_m q \, dx = \hat{u}_{k,j+\frac{1}{2}} v_{m,j+\frac{1}{2}} - \hat{u}_{k,j-\frac{1}{2}} v_{m,j-\frac{1}{2}} - \int_{\Omega_j} \frac{\partial v_m}{\partial x} u_k \, dx, \tag{48a}$$

$$\int_{\Omega_j} v_m p \, dx = \hat{q}_{j+\frac{1}{2}} v_{m,j+\frac{1}{2}} - \hat{q}_{j-\frac{1}{2}} v_{m,j-\frac{1}{2}} - \int_{\Omega_j} \frac{\partial v_m}{\partial x} q \, dx, \tag{48b}$$

$$\int_{\Omega_j} v_m r \, dx = \hat{p}_{j+\frac{1}{2}} v_{m,j+\frac{1}{2}} - \hat{p}_{j-\frac{1}{2}} v_{m,j-\frac{1}{2}} - \int_{\Omega_j} \frac{\partial v_m}{\partial x} p \, dx, \tag{48c}$$

$$\int_{\Omega_j} v_m \frac{\partial u_k}{\partial t} \, dx = -\int_{\Omega_j} v_m r \, dx + \hat{f}(u_k^-, u_k^+)_{j+\frac{1}{2}} v_{m,j+\frac{1}{2}} - \hat{f}(u_k^-, u_k^+)_{j-\frac{1}{2}} v_{m,j-\frac{1}{2}} - \int_{\Omega_j} \frac{\partial v_m}{\partial x} f(u_k) \, dx + \epsilon \eta_k \int_{\Omega_j} v_m \, dx, \tag{48d}$$

Here $\hat{u}_{j\pm\frac{1}{2}}$, $\hat{q}_{j\pm\frac{1}{2}}$ and $\hat{p}_{j\pm\frac{1}{2}}$ are the so-called "interface fluxes" between domains Ω_j and $\Omega_{j\pm1}$. We choose the fluxes based on upwind principles [24],

$$\begin{aligned} &\hat{u}_{j\pm\frac{1}{2}} = u^-_{j\pm\frac{1}{2}}, \quad \hat{p}_{j\pm\frac{1}{2}} = p^+_{j\pm\frac{1}{2}}, \\ &\hat{q}_{j\pm\frac{1}{2}} = \frac{q^+_{j\pm\frac{1}{2}} + q^-_{j\pm\frac{1}{2}}}{2}. \end{aligned} \tag{49}$$

The '+' or '−' superscript defines whether the function is computed from the right side of the interface or from the left side. Taking values of the evaluated functions from the outer side of the interface is equivalent to imposing boundary condition for element Ω_j. The values of the test functions are always computed from the inner sides of the interfaces of the sub-domain Ω_j. Choosing upwind fluxes guarantees stability and convergence, see proofs in [24]. In Eq. (48d), $\hat{f}(u_k^-, u_k^+)$ is a monotone flux for $f(u_k)$. We use the simple Lax–Friedrichs flux,

$$\hat{f}(u_k^-, u_k^+) = \frac{1}{2}(f(u_k^-) + f(u_k^+) - \alpha(u_k^+ - u_k^-)), \quad \alpha = \max_{u_k} |f'(u_k)|, \tag{50}$$

where $f(u_k) = \frac{3}{e_{0,k,k}} \sum_{s=0}^{M} \sum_{l=0}^{M} u_s u_l e_{s,l,k}$ and the maximum is taken over Ω_j. By integrating by parts again, the weak form Eqs. (48a)–(48d) can be represented as

$$\int_{\Omega_j} v_m q \, dx = v_{m,j-\frac{1}{2}}(u^+_{k,j-\frac{1}{2}} - u^-_{k,j-\frac{1}{2}}) + \int_{\Omega_j} \frac{\partial u_k}{\partial x} v_m \, dx, \tag{51a}$$

$$\int_{\Omega_j} v_m p \, dx = v_{m,j+\frac{1}{2}} \frac{(q^+_{j+\frac{1}{2}} - q^-_{j+\frac{1}{2}})}{2} - v^+_{m,j-\frac{1}{2}} \frac{(q^-_{j-\frac{1}{2}} - q^+_{j-\frac{1}{2}})}{2} + \int_{\Omega_j} \frac{\partial q}{\partial x} v_m \, dx, \tag{51b}$$

$$\int_{\Omega_j} v_m r \, dx = v_{m,j+\frac{1}{2}}(p^+_{j+\frac{1}{2}} - p^-_{j+\frac{1}{2}}) + \int_{\Omega_j} \frac{\partial q}{\partial x} v_m \, dx, \tag{51c}$$

$$\int_{\Omega_j} v_m \frac{\partial u_k}{\partial t} \, dx = -\int_{\Omega_j} v_m r \, dx + \hat{f}(u_k^-, u_k^+)_{j+\frac{1}{2}} v_{m,j+\frac{1}{2}} - \hat{f}(u_k^-, u_k^+)_{j-\frac{1}{2}} v_{m,j-\frac{1}{2}} - \int_{\Omega_j} \frac{\partial v_m}{\partial x} f(u_k) \, dx + \epsilon \eta_k \int_{\Omega_j} v_m \, dx. \tag{51d}$$

In each spectral element Ω_j, we employ Legendre expansions for all variables of the form:

$$u_k(x,t) \simeq \sum_{l=0}^{P_j} U_{k,l}(t) \Psi_l(x), \tag{52}$$

where $\Psi_l(x)$ are the Legendre polynomials of order l and $U_{k,l}(t)$ are their coefficients. P_j is the highest order of the Legendre polynomials on element j. To improve the efficiency, we can adaptively choose

appropriate P_j for each element j. Integrals in Eqs. (51a)–(51d) generate the mass matrix, $\mathbf{M}$, and the advection operator, $\mathbf{L}$,

$$\mathbf{M} = \int_{\Omega_j} \mathbf{V} \cdot \mathbf{\Psi}^{\mathrm{T}} \, \mathrm{d}x, \quad \mathbf{L} = \int_{\Omega_j} \mathbf{V} \cdot \left(\frac{\partial \mathbf{\Psi}}{\partial x} \right)^{\mathrm{T}} \mathrm{d}x, \tag{53}$$

where $\mathbf{V} = \{v_m\}$, $\mathbf{\Psi} = \{\Psi_l\}$ $(m, l = 0, \ldots, P_j)$. The orthogonal properties of the Legendre polynomials lead to the diagonal mass matrix, $\mathbf{M}$, which dramatically lowers the computational cost. The advection operator, $\mathbf{L}$, is a sparse upper triangular matrix and all its nonzero entries are equal to 2, which contributes to an additional computational cost reduction. By transforming Eqs. (51a)–(51d) into a matrix form, we get,

$$\hat{Q} = \mathbf{M}^{-1}[\mathbf{V}_{j-\frac{1}{2}}(u^{+}_{k,j-\frac{1}{2}} - u^{-}_{k,j-\frac{1}{2}}) + \mathbf{L}\hat{U}_k], \tag{54a}$$

$$\hat{P} = \mathbf{M}^{-1}\left[\mathbf{V}_{j+\frac{1}{2}} \frac{(q^{+}_{j+\frac{1}{2}} - q^{-}_{j+\frac{1}{2}})}{2} - \mathbf{V}_{j-\frac{1}{2}} \frac{(q^{-}_{j-\frac{1}{2}} - q^{+}_{j-\frac{1}{2}})}{2} + \mathbf{L}\hat{Q}\right], \tag{54b}$$

$$\hat{R} = \mathbf{M}^{-1}[\mathbf{V}_{j+\frac{1}{2}}(p^{+}_{j+\frac{1}{2}} - p^{-}_{j+\frac{1}{2}}) + \mathbf{L}\hat{P}], \tag{54c}$$

$$\frac{\partial \hat{U}_k}{\partial t} = -\hat{R} + \mathbf{M}^{-1}\left[\hat{f}(u^{-}_k, u^{+}_k)_{j+\frac{1}{2}}\mathbf{V}_{j+\frac{1}{2}} - \hat{f}(u^{-}_k, u^{+}_k)_{j-\frac{1}{2}}\mathbf{V}_{j-\frac{1}{2}} - \int_{\Omega_j} \frac{\partial \mathbf{V}}{\partial x} f(u_k) \, \mathrm{d}x + \epsilon\eta_k \int_{\Omega_j} \mathbf{V} \, \mathrm{d}x\right], \tag{54d}$$

where $\hat{U}_k = \{U_{k,l}\}, \hat{Q} = \{Q_l\}, \hat{P} = \{P_l\}, \hat{R} = \{R_l\}, (l = 0, \ldots, P_j)$. Similarly, by setting $\epsilon = 0$, we derive the stochastic DG method for one-dimensional space-dependent stochastic KdV for Eq. (1):

$$\hat{Q} = \mathbf{M}^{-1}[\mathbf{V}_{j-\frac{1}{2}}(u^{+}_{k,j-\frac{1}{2}} - u^{-}_{k,j-\frac{1}{2}}) + \mathbf{L}\hat{U}_k], \tag{55a}$$

$$\hat{P} = \mathbf{M}^{-1}\left[\mathbf{V}_{j+\frac{1}{2}} \frac{(q^{+}_{j+\frac{1}{2}} - q^{-}_{j+\frac{1}{2}})}{2} - \mathbf{V}_{j-\frac{1}{2}} \frac{(q^{-}_{j-\frac{1}{2}} - q^{+}_{j-\frac{1}{2}})}{2} + \mathbf{L}\hat{Q}\right], \tag{55b}$$

$$\hat{R} = \mathbf{M}^{-1}[\mathbf{V}_{j+\frac{1}{2}}(p^{+}_{j+\frac{1}{2}} - p^{-}_{j+\frac{1}{2}}) + \mathbf{L}\hat{P}], \tag{55c}$$

$$\frac{\partial \hat{U}_k}{\partial t} = -\hat{R} + \mathbf{M}^{-1}\left[\hat{f}(u^{-}_k, u^{+}_k)_{j+\frac{1}{2}}\mathbf{V}_{j+\frac{1}{2}} - \hat{f}(u^{-}_k, u^{+}_k)_{j-\frac{1}{2}}\mathbf{V}_{j-\frac{1}{2}} - \int_{\Omega_j} \frac{\partial \mathbf{V}}{\partial x} f(u_k) \, \mathrm{d}x - F_{\mathrm{r}}\right], \tag{55d}$$

where

$$F_{\mathrm{r}} = \frac{\mathbf{V}_{j-\frac{1}{2}}}{e_{0,k,k}} \sum_{s=0}^{N} \sum_{l=0}^{M} v\zeta_{s,j-\frac{1}{2}}(u^{+}_{l,j-\frac{1}{2}} - u^{-}_{l,j-\frac{1}{2}}) e_{s,l,k} + \int_{\Omega_j} \frac{\mathbf{V}}{e_{0,k,k}} \sum_{s=0}^{N} \sum_{l=0}^{M} v\zeta_{\mathrm{s}} \frac{\partial u_l}{\partial x} e_{s,l,k} \, \mathrm{d}x$$

Based on the the finite difference scheme in [25], the second-order stochastic FD method for the one-dimensional time-dependent stochastic KdV equation gives:

$$\begin{aligned} u^{n+1}_{k,j} = {} & u^{n}_{k,j} + \frac{3\lambda}{2e_{0,k,k}} \sum_{s=0}^{M} \sum_{l=0}^{M} e_{s,l,k}[(u^{n}_{s,j+1})(u^{n}_{l,j+1}) - (u^{n}_{s,j-1})(u^{n}_{l,j-1})] - \frac{\lambda}{2(\Delta x)^2}(u^{n}_{k,j+2} - 2u^{n}_{k,j+1} + 2u^{n}_{k,j-1} - u^{n}_{k,j-2}) \\ & - \frac{3\lambda^2}{e_{0,k,k}} \sum_{s=0}^{M} \sum_{l=0}^{M} e_{s,l,k}[(u^{n}_{s,j+1} + u^{n}_{s,j})(u^{n}_{l,j+1} - u^{n}_{l,j}) - (u^{n}_{s,j} + u^{n}_{s,j-1})(u^{n}_{l,j} - u^{n}_{l,j-1})] \\ & - \frac{6\lambda}{e_{0,k,k}(\Delta x)^2} \sum_{s=0}^{M} \sum_{l=0}^{M} e_{s,l,k}[u^{n}_{s,j}(u^{n}_{l,j+2} - 4u^{n}_{l,j+1} + 6u^{n}_{l,j} - 4u^{n}_{l,j-1} + u^{n}_{l,j-2})] \\ & + \frac{\lambda^2}{2(\Delta x)^4}(u^{n}_{k,j+3} - 6u^{n}_{k,j+2} + 15u^{n}_{k,j+1} - 20u^{n}_{k,j} + 15u^{n}_{k,j-1} - 6u^{n}_{k,j-2} + u^{n}_{k,j-3}) + \epsilon\eta_k \Delta t, \end{aligned} \tag{56}$$

where $\lambda = \frac{\Delta t}{\Delta x}$. Similarly, we can employ the stochastic second-order FD method for the one-dimensional space-dependent stochastic KdV equation as follows:

$$
\begin{aligned}
u_{k,j}^{n+1} = {} & u_{k,j}^{n} - \frac{\lambda}{2e_{0,k,k}} \sum_{s=0}^{M} \sum_{l=0}^{M} e_{s,l,k}[u_{s,j+1}^{n}(v\zeta_{l,j} - 3u_{l,j+1}^{n}) - u_{s,j-1}^{n}(v\zeta_{l,j} - 3u_{l,j-1}^{n})] \\
& - \frac{\lambda}{2(\Delta x)^2}(u_{k,j+2}^{n} - 2u_{k,j+1}^{n} + 2u_{k,j-1}^{n} - u_{k,j-2}^{n}) + \frac{\lambda^2}{2e_{0,k,k}} \sum_{s=0}^{N} \sum_{l=0}^{M} e_{s,l,k} v\zeta_{s,j}(u_{l,j+1}^{n} - 2u_{l,j}^{n} + u_{l,j-1}^{n}) \\
& - \frac{3\lambda^2}{e_{0,k,k}} \sum_{s=0}^{M} \sum_{l=0}^{M} e_{s,l,k}[(u_{s,j+1}^{n} + u_{s,j}^{n})(u_{l,j+1}^{n} - u_{l,j}^{n}) - (u_{s,j}^{n} + u_{s,j-1}^{n})(u_{l,j}^{n} - u_{l,j-1}^{n})] \\
& + \frac{\lambda}{e_{0,k,k}(\Delta x)^2} \sum_{s=0}^{M} \sum_{l=0}^{M} e_{s,l,k}[(v\zeta_{s,j} - 6u_{s,j}^{n})(u_{l,j+2}^{n} - 4u_{l,j+1}^{n} + 6u_{l,j}^{n} - 4u_{l,j-1}^{n} + u_{l,j-2}^{n})] \\
& + \frac{\lambda^2}{2(\Delta x)^4}(u_{k,j+3}^{n} - 6u_{k,j+2}^{n} + 15u_{k,j+1}^{n} - 20u_{k,j}^{n} + 15u_{k,j-1}^{n} - 6u_{k,j-2}^{n} + u_{k,j-3}^{n}).
\end{aligned} \tag{57}
$$

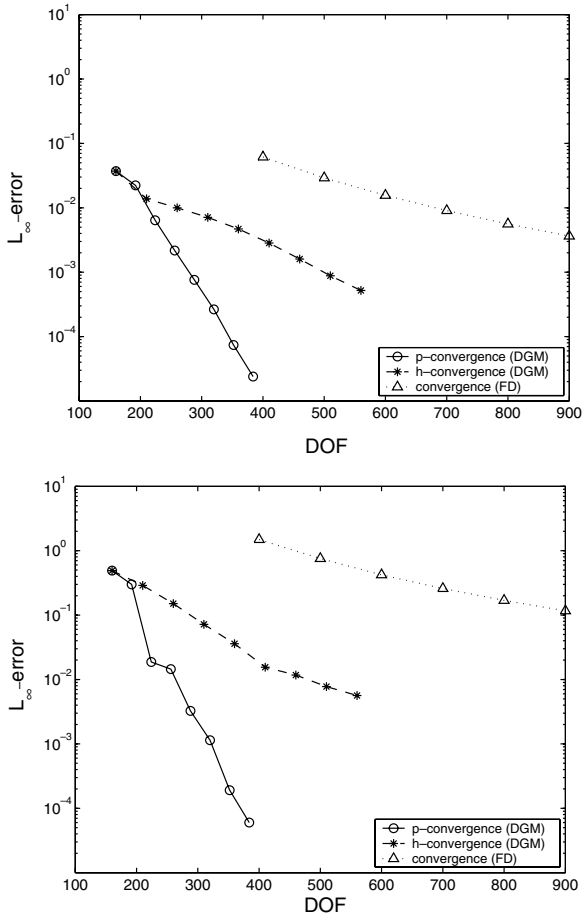

Fig. 29. Convergence rates of the deterministic solvers at $t = 1$ (upper figure) and $t = 5$ (lower figure).

Table 1
L_∞ errors at $t = 1$, obtained by the DG methods for a stochastic solver for Eq. (1) ($v = 0, \epsilon = 0.1$, η is a Gaussian random variable) and a deterministic solver for Eq. (1) ($v = 0, \epsilon = 0$)

Degree of freedom	210	252	294	336
L_∞ errors (stochastic DG)	1.786e − 2	1.1375e − 2	1.8513e − 3	6.6864e − 4
L_∞ errors (deterministic DG)	2.154e − 2	1.3828e − 2	2.37e − 3	7.7313e − 4

Table 2
L_∞ errors at $t = 1$ obtained by the second-order FD methods as a stochastic solver for Eq. (1) ($v = 0, \epsilon = 0.1$, η is a Gaussian random variable) and a deterministic solver for Eq. (1) ($v = 0, \epsilon = 0$) at $t = 1$

Degree of freedom	400	500	600	700
L_∞ errors (stochastic FD)	0.0566388	0.0274777	0.0146638	0.00902784
L_∞ errors (deterministic FD)	0.0613785	0.0291867	0.0156231	0.00905615

Appendix B. Accuracy of the deterministic and stochastic solvers

The stochastic and deterministic KdV equations have been solved numerically using the DG method and the second-order FD method. In the following simulations, the time step, Δt, is chosen such that the temporal numerical error is negligible ($\Delta t \sim 10^{-6}$), compared to spatial numerical error. In order to study the accuracy of the DG solver, the size of the sub-domain, Ω_j, and the maximum polynomial order, P_j, are kept constant for all j elements. Next, we will compare the spatial accuracy of the two methods in the deterministic ($v = \epsilon = 0$) and stochastic cases ($v = 0, \epsilon = 0.1$, $\eta \sim$ Gaussian random variable) and investigate how the stochastic error and the spatial discretization error will affect the overall accuracy of the corresponding solution. As an estimate for the numerical error, we use $L_\infty = \mathrm{Max}|u_{\mathrm{exact}} - u_{num}|$ and we define the degrees of freedom (DOF) as $\mathrm{DOF} = \sum_{j=1}^{N_{\mathrm{el}}} (P_j + 1)$ for the DG method and DOF is equal to the number of grid points for FD method. In Fig. 29, we compare the convergence rates of the two deterministic solvers: the DG method and the second-order FD scheme at $t = 1$ and 5. It is obvious that the DG method has better convergence rate than the second-order FD method. By comparing the numerical error of the two methods at $t = 1$ and 5, we can see that the second-order FD method accumulates error much faster than the DG method.

In Tables 1 and 2, we present the L_∞ errors of stochastic mean and deterministic solutions at $t = 1$ obtained by the DG method and the second-order FD method. The same magnitude is observed between the L_∞ errors of the two stochastic solvers and the L_∞ errors of the two deterministic solvers. This verifies the accuracy of our stochastic solvers and proves that we can reach the same high accuracy as solving deterministic equations, by choosing high order stochastic expansions.

References

[1] H. Washimi, T. Taniuti, Propagation of ion-acoustic solitary waves of small amplitude, Phys. Rev. Lett. 17 (1966) 996–998.
[2] M. Wadati, Stochastic Korteweg-de Vries equation, J. Phys. Soc. Jpn. 52 (8) (1983) 2642–2648.
[3] R.L. Herman, The stochastic, damped KdV equation, J. Phys. A (1990) 1063–1084.
[4] A. Debussche, J. Printems, Numerical simulation of the stochastic Korteweg-de Vries equation, Physica D 134 (1999) 200–226.
[5] J. Garnier, Solitons in random media with long-range correlation, Waves Random Media 11 (2001) 149–162.
[6] J. Garnier, Long-time dynamics of Korteweg-de Vries solitons driven by random perturbations, J. Stat. Phys. 105 (516) (1993) 789–833.
[7] N. Zabusky, M. Kruskal, Interaction of solitions in a collisionless plasma and the recurrence of initial states, Phys. Rev. Lett. 15 (1965) 240–243.
[8] C. Gardner, J. Greene, M. Kruskal, R. Miura, Method for solving the Korteweg-de Vries equation, Phys. Rev. Lett. 19 (1967) 1095–1097.
[9] M. Wadati, Y. Akutsu, Stochastic Korteweg-de Vries equation with and without damping, J. Phys. Soc. Jpn. 53 (1984) 3342–3350.
[10] T. Iizuka, Anomalous diffusion of solitons in random systems, Phys. Rev. Lett. 181 (1993) 39–42.
[11] M. Scalerandi, A. Romano, Korteweg-de Vries equation under additive stochastic perturbations, Phys. Rev. E 58 (4) (1998) 4166–4173.

[12] F. Calogero, A. Degasperis, Solitons and the Spectral Transform I, North-Holland, Amsterdam, 1982.
[13] G.L. Lamb Jr., Elements of Soliton Theory, Wiley, London, 1980.
[14] M. Ablowitz, H. Segur, Solitons and the Inverse Scattering Transform, SIAM, Philadelphia, 1981.
[15] L. Faddeev, L. Takhtajan, Hamiltonian Methods in the Theory of Solitons, Springer, Berlin, 1987.
[16] R. Dodd, J. Eilbeck, J. Gibbon, H. Morris, Solitons and Nonlinear Wave Equations, Academic Press, London, 1982.
[17] A. Newell, Solitons in Mathematics and Physics, SIAM, Philadelphia, 1985.
[18] V. Konotop, L. Vazquez, Nonlinear Random Waves, World Scientific, Singapore, 1994.
[19] S. Novikov, L.P.S.V. Manakov, V. Zakharov, Theory of Solitons: Inverse Scattering Method, Consultants Bureau, New York, 1980.
[20] N. Wiener, The homogeneous chaos, Am. J. Math. 60 (1938) 897–936.
[21] R.G. Ghanem, P. Spanos, Stochastic Finite Elements: A Spectral Approach, Springer, New York, 1991.
[22] D. Xiu, G.E. Karniadakis, The Wiener–Askey polynomial chaos for stochastic differential equations, SIAM J. Sci. Comput. 24 (2) (2002) 619–644.
[23] B. Cockburn, G.E. Karniadakis, C.-W. Shu, The development of discontinuous Galerkin methods, Discontinuous Galerkin Methods: Theory, Computations and Applications, Springer, Berlin, 2000.
[24] J. Yan, C.-W. Shu, A local discontinuous Galerkin method for KdV type equations, SIAM J. Numer. Anal. 40 (2) (2002) 769–791.
[25] A.C. Vliegenthart, On finite-difference methods for the Korteweg-de Vries equation, J. Eng. Math. 5 (2) (1971) 137–155.
[26] G. Lin, C. Su, G. Karniadakis, The stochastic piston problem, Proc. Natl. Acad. Sci. USA 101 (45) (2004) 15840–15845.
[27] X. Wan, G.E. Karniadakis, An adaptive multi-element generalized polynomial chaos method for stochastic differential equations, J. Comput. Phys. 209 (2005) 617–642.
[28] D. Lucor, C.-H. Su, G.E. Karniadakis, Karhunen–Loeve representation of periodic second-order autoregressive processes, in: International Conference on Computational Science, Krakow, Poland, 2004.